Solar neutrino measurements in Super-Kamiokande-IV

K. Abe,[1,32] Y. Haga,[1] Y. Hayato,[1,32] M. Ikeda,[1] K. Iyogi,[1] J. Kameda,[1,32] Y. Kishimoto,[1,32] Ll. Marti,[1] M. Miura,[1,32]
S. Moriyama,[1,32] M. Nakahata,[1,32] T. Nakajima,[1] S. Nakayama,[1,32] A. Orii,[1] H. Sekiya,[1,32] M. Shiozawa,[1,32] Y. Sonoda,[1]
A. Takeda,[1,32] H. Tanaka,[1] Y. Takenaga,[1] S. Tasaka,[1] T. Tomura,[1] K. Ueno,[1] T. Yokozawa,[1] R. Akutsu,[2] T. Irvine,[2] H. Kaji,[2]
T. Kajita,[2,32] I. Kametani,[2] K. Kaneyuki,[2,32,*] K. P. Lee,[2] Y. Nishimura,[2] T. McLachlan,[2] K. Okumura,[2,32] E. Richard,[2]
L. Labarga,[3] P. Fernandez,[3] F. d. M. Blaszczyk,[4] J. Gustafson,[4] C. Kachulis,[4] E. Kearns,[4,32] J. L. Raaf,[4] J. L. Stone,[4,32]
L. R. Sulak,[4] S. Berkman,[5] S. Tobayama,[5] M. Goldhaber,[6,*] K. Bays,[7] G. Carminati,[7] N. J. Griskevich,[7] W. R. Kropp,[7]
S. Mine,[7] A. Renshaw,[7] M. B. Smy,[7,32] H. W. Sobel,[7,32] V. Takhistov,[7] P. Weatherly,[7] K. S. Ganezer,[8] B. L. Hartfiel,[8] J. Hill,[8]
W. E. Keig,[8] N. Hong,[9] J. Y. Kim,[9] I. T. Lim,[9] R. G. Park,[9] T. Akiri,[10] J. B. Albert,[10] A. Himmel,[10] Z. Li,[10] E. O'Sullivan,[10]
K. Scholberg,[10,32] C. W. Walter,[10,32] T. Wongjirad,[10] T. Ishizuka,[11] T. Nakamura,[12] J. S. Jang,[13] K. Choi,[14] J. G. Learned,[14]
S. Matsuno,[14] S. N. Smith,[14] M. Friend,[15] T. Hasegawa,[15] T. Ishida,[15] T. Ishii,[15] T. Kobayashi,[15] T. Nakadaira,[15]
K. Nakamura,[15,32] K. Nishikawa,[15] Y. Oyama,[15] K. Sakashita,[15] T. Sekiguchi,[15] T. Tsukamoto,[15] Y. Nakano,[16]
A. T. Suzuki,[16] Y. Takeuchi,[16,32] T. Yano,[16] S. V. Cao,[17] T. Hayashino,[17] T. Hiraki,[17] S. Hirota,[17] K. Huang,[17] K. Ieki,[17]
M. Jiang,[17] T. Kikawa,[17] A. Minamino,[17] A. Murakami,[17] T. Nakaya,[17,32] N. D. Patel,[17] K. Suzuki,[17] S. Takahashi,[17]
R. A. Wendell,[17,32] Y. Fukuda,[18] Y. Itow,[19,20] G. Mitsuka,[19] F. Muto,[19] T. Suzuki,[19] P. Mijakowski,[21] K. Frankiewicz,[21]
J. Hignight,[22] J. Imber,[22] C. K. Jung,[22] X. Li,[22] J. L. Palomino,[22] G. Santucci,[22] I. Taylor,[22] C. Vilela,[22] M. J. Wilking,[22]
C. Yanagisawa,[22,†] D. Fukuda,[23] H. Ishino,[23] T. Kayano,[23] A. Kibayashi,[23] Y. Koshio,[23,32] T. Mori,[23] M. Sakuda,[23]
J. Takeuchi,[23] R. Yamaguchi,[23] Y. Kuno,[24] R. Tacik,[25,34] S. B. Kim,[26] H. Okazawa,[27] Y. Choi,[28] K. Ito,[29] K. Nishijima,[29]
M. Koshiba,[30] Y. Totsuka,[30,*] Y. Suda,[31] M. Yokoyama,[31,32] C. Bronner,[32] R. G. Calland,[32] M. Hartz,[32] K. Martens,[32]
Y. Obayashi,[32] Y. Suzuki,[32] M. R. Vagins,[32,7] C. M. Nantais,[33] J. F. Martin,[33] P. de Perio,[33] H. A. Tanaka,[33] A. Konaka,[34]
S. Chen,[35] H. Sui,[35] L. Wan,[35] Z. Yang,[35] H. Zhang,[35] Y. Zhang,[35] K. Connolly,[36] M. Dziomba,[36] and R. J. Wilkes[36]

(Super-Kamiokande Collaboration)

[1]*Kamioka Observatory, Institute for Cosmic Ray Research, University of Tokyo,
Kamioka, Gifu 506-1205, Japan*
[2]*Research Center for Cosmic Neutrinos, Institute for Cosmic Ray Research,
University of Tokyo, Kashiwa, Chiba 277-8582, Japan*
[3]*Department of Theoretical Physics, University Autonoma Madrid, 28049 Madrid, Spain*
[4]*Department of Physics, Boston University, Boston, Massachusetts 02215, USA*
[5]*Department of Physics and Astronomy, University of British Columbia,
Vancouver, British Columbia V6T1Z4, Canada*
[6]*Physics Department, Brookhaven National Laboratory, Upton, New York 11973, USA*
[7]*Department of Physics and Astronomy, University of California,
Irvine, Irvine, California 92697-4575, USA*
[8]*Department of Physics, California State University, Dominguez Hills, Carson, California 90747, USA*
[9]*Department of Physics, Chonnam National University, Kwangju 500-757, Korea*
[10]*Department of Physics, Duke University, Durham North Carolina 27708, USA*
[11]*Junior College, Fukuoka Institute of Technology, Fukuoka, Fukuoka 811-0295, Japan*
[12]*Department of Physics, Gifu University, Gifu, Gifu 501-1193, Japan*
[13]*GIST College, Gwangju Institute of Science and Technology, Gwangju 500-712, Korea*
[14]*Department of Physics and Astronomy, University of Hawaii, Honolulu, Hawaii 96822, USA*
[15]*High Energy Accelerator Research Organization (KEK), Tsukuba, Ibaraki 305-0801, Japan*
[16]*Department of Physics, Kobe University, Kobe, Hyogo 657-8501, Japan*
[17]*Department of Physics, Kyoto University, Kyoto, Kyoto 606-8502, Japan*
[18]*Department of Physics, Miyagi University of Education, Sendai, Miyagi 980-0845, Japan*
[19]*Institute for Space-Earth Enviromental Research, Nagoya University, Nagoya, Aichi 464-8602, Japan*
[20]*Kobayashi-Maskawa Institute for the Origin of Particles and the Universe,
Nagoya University, Nagoya, Aichi 464-8602, Japan*
[21]*National Centre For Nuclear Research, 00-681 Warsaw, Poland*
[22]*Department of Physics and Astronomy, State University of New York at Stony Brook,
New York 11794-3800, USA*
[23]*Department of Physics, Okayama University, Okayama, Okayama 700-8530, Japan*
[24]*Department of Physics, Osaka University, Toyonaka, Osaka 560-0043, Japan*
[25]*Department of Physics, University of Regina, 3737 Wascana Parkway, Regina,
Saskatchewan S4SOA2, Canada*

^{26}*Department of Physics, Seoul National University, Seoul 151-742, Korea*
^{27}*Department of Informatics in Social Welfare, Shizuoka University of Welfare,*
Yaizu, Shizuoka, 425-8611, Japan
^{28}*Department of Physics, Sungkyunkwan University, Suwon 440-746, Korea*
^{29}*Department of Physics, Tokai University, Hiratsuka, Kanagawa 259-1292, Japan*
^{30}*The University of Tokyo, Bunkyo, Tokyo 113-0033, Japan*
^{31}*Department of Physics, University of Tokyo, Bunkyo, Tokyo 113-0033, Japan*
^{32}*Kavli Institute for the Physics and Mathematics of the Universe (WPI), The University of Tokyo Institutes*
for Advanced Study, University of Tokyo, Kashiwa, Chiba 277-8583, Japan
^{33}*Department of Physics, University of Toronto, 60 St., Toronto, Ontario M5S1A7, Canada*
^{34}*TRIUMF, 4004 Wesbrook Mall, Vancouver, British Columbia V6T2A3, Canada*
^{35}*Department of Engineering Physics, Tsinghua University, Beijing 100084, China*
^{36}*Department of Physics, University of Washington, Seattle, Washington 98195-1560, USA*

Upgraded electronics, improved water system dynamics, better calibration and analysis techniques allowed Super-Kamiokande-IV to clearly observe very low-energy ^{8}B solar neutrino interactions, with recoil electron kinetic energies as low as $\sim$3.5 MeV. Super-Kamiokande-IV data-taking began in September of 2008; this paper includes data until February 2014, a total livetime of 1664 days. The measured solar neutrino flux is $(2.308 \pm 0.020(\text{stat})^{+0.039}_{-0.040}(\text{syst})) \times 10^6/(\text{cm}^2 \text{ sec})$ assuming no oscillations. The observed recoil electron energy spectrum is consistent with no distortions due to neutrino oscillations. An extended maximum likelihood fit to the amplitude of the expected solar zenith angle variation of the neutrino-electron elastic scattering rate in SK-IV results in a day/night asymmetry of $(-3.6 \pm 1.6(\text{stat}) \pm 0.6(\text{syst}))\%$. The SK-IV solar neutrino data determine the solar mixing angle as $\sin^2\theta_{12} = 0.327^{+0.026}_{-0.031}$, all SK solar data (SK-I, SK-II, SK III and SK-IV) measures this angle to be $\sin^2\theta_{12} = 0.334^{+0.027}_{-0.023}$, the determined mass-squared splitting is $\Delta m^2_{21} = 4.8^{+1.5}_{-0.8} \times 10^{-5}$ eV^2.

I. INTRODUCTION

Solar neutrino flux measurements from Super-Kamiokande (SK) [1] and the Sudbury Neutrino Observatory (SNO) [2] have provided clear evidence for solar neutrino flavor conversion in which electron flavor neutrinos convert to either muon or tau flavor neutrinos. This flavor conversion is well described by flavor oscillations of three neutrinos. In particular, the extracted oscillation parameters agree with nuclear reactor antineutrino measurements [3]. However, while oscillations of reactor antineutrinos at the solar frequency were observed, there is still no clear evidence that the solar neutrino flavor conversion is indeed due to neutrino oscillations and not caused by another mechanism. Currently there are two types of testable signatures unique to neutrino oscillations, the first being the observation and precision test of the Mikheyev–Smirnov–Wolfenstein (MSW) resonance curve [4], the characteristic energy dependence of the flavor conversion (assuming oscillation parameters extracted from solar neutrino and reactor antineutrino measurements): higher energy solar neutrinos (higher energy ^{8}B and *hep* neutrinos) undergo adiabatic resonant conversion within the Sun (present data imply a

survival probability of about 30%), while the flavor changes of the lower energy solar neutrinos (pp, ^{7}Be, pp, CNO and lower energy ^{8}B neutrinos) arise only from vacuum oscillations. These averaged vacuum oscillations lead to an average survival probability which—for sufficiently small 1–3 mixing—must exceed 50% (present data imply about 60%). The transition from the matter-dominated oscillations within the Sun to the vacuum-dominated oscillations should occur near three MeV. This makes ^{8}B neutrinos the best choice when looking for a transition point within the energy spectrum. An observed deviation from the expected behavior in the transition region would imply new physics, e.g. nonstandard interactions [5] or mass-varying neutrinos [6]. A second signature unique to oscillations arises from the effect of the terrestrial matter density on solar neutrino oscillations. This effect is tested directly by comparing solar neutrinos that pass long distances through the Earth at nighttime to those which do not pass through the Earth during the daytime. Those neutrinos which pass through the Earth will generally have an enhanced electron neutrino content, leading to an increase in the nighttime electron elastic scattering rate (or any charged-current interaction rate), and hence a negative "day/night asymmetry" $(r_D - r_N)/r_{\text{ave}}$, where r_D (r_N) is the daytime (nighttime) rate and $r_{\text{ave}} = \frac{1}{2}(r_D + r_N)$ is the average rate. This day/night asymmetry depends on the solar mass squared splitting and therefore

constitutes a measurement of this oscillation parameter. It is also sensitive to new physics. SK is sensitive to ^{8}B and hep solar neutrinos in the energy range around 4 to 18.7 MeV and precisely measures the neutrino interaction time. It is therefore a good detector to search for both solar neutrino oscillation signatures.

SK [7] is a large, cylindrical, water Cherenkov detector containing 50,000 tons of ultrapure water. It is located 1,000 m beneath the peak of Mount Ikenoyama, in Kamioka Town, Japan. The SK detector is optically separated into a 32.5 kton cylindrical inner detector (ID) surrounded by a ~2.5 meter water shield, ~2 m of which is the active veto outer detector (OD). The structure dividing the detector regions contains an array of photomultiplier tubes (PMTs). SK started data-taking in April of 1996, with 11,146 ID and 1,885 OD PMTs, and was then shut down for maintenance in June of 2001. This period is called SK-I [1]. While refilling the tank with water in November of 2001, a PMT implosion caused a chain reaction which destroyed 60% of the PMTs. The surviving and new PMTs were redistributed and covered with fiber-reinforced plastic (FRP) and acrylic cases, in order to avoid another accidental chain reaction. Data-taking restarted with 5,182 ID and 1,885 OD PMTs in December of 2002, and the period until October of 2005 is called SK-II [8]. In October of 2006, newly manufactured PMTs replaced those which had been destroyed, and with 11,129 ID and 1,885 OD PMTs data-taking resumed as the SK-III phase [9]. The fourth phase of SK (SK-IV) began in September of 2008, with new front-end electronics (QTC Based Electronics with Ethernet, QBEE [10]) for both the ID and OD, new data acquisition system, and continues to this day. This paper will include data taken up until the beginning of February 2014.

Improvements in the front-end electronics, the water circulation system, calibration techniques and the analysis methods have allowed the SK-IV solar neutrino measurements to be made with a lower energy threshold and smaller systematic uncertainties, compared to SK-I, II and III. The hardware and software improvements are summarized in Sec. II, while the SK-IV data set, data reduction, and its systematic uncertainty estimations on the total flux are detailed in Sec. III. The simulation of solar neutrino events in SK is described also in Sec. III. Unfortunately, the simulation code for the SK-III period used in [9] was inaccurate, which affected the input recoil electron spectrum. The details (and the correction applied) as well as a reanalysis of the SK-III data are briefly described in Sec. III and Appendix A.

In Sec. IV, the energy spectrum results of SK-IV as well as all SK phases combined are discussed. Section V presents the SK-IV day/night asymmetry analysis. Finally, Sec. VI contains an oscillation analysis of SK-IV data by themselves and in combination with other SK phases, and also a global analysis which combines the SK results with other relevant experiments.

In previous SK solar neutrino publications [1,8,9] "energy" meant total recoil electron energy, while in this paper we subtract the electron mass $m_e = 511$ keV to obtain kinetic energy. The kinetic energy threshold of the SK-IV data analysis is thus 3.49 MeV, corresponding to the total energy of 4.00 MeV.

II. DETECTOR PERFORMANCE

A. Electronics, data acquisition system

To ensure stable observation and to improve the sensitivity of the detector, new front-end electronics called QBEEs were installed, allowing for the development of a new online data acquisition system. The essential components on the QBEEs used for the analog signal processing and digitization are the QTC (high-speed charge-to-time converter) ASICs [10], which achieve very high speed signal processing and allow the integration of the charge and recording of the time of every PMT signal. These PMT signal times and charge integrals are sent to online computers, where a software trigger searches for timing coincidences within 200 ns to pick out events in a similar fashion as the hardware "hitsum trigger" did in SK-I through III [1,8,9]. The energy threshold of this coincidence trigger is determined by the number of coincident PMT signals that are required: a smaller coincidence level will be more sensitive to lower energy events, but will result in larger event rates. The definitions of the different trigger types and the corresponding typical event rates are summarized in Table I. Since all PMT signals are digitized and recorded, there is no deadtime of the detector from a large trigger rate, so the efficiency of triggering on HE events does not limit the maximum possible rate of SLE triggers; only the processing capability of the online computers limits this maximum rate. The software trigger system uses flexible event time periods (1.3 μ sec for SLE, 40 μ sec for LE and HE). The trigger efficiencies for the thresholds are ~84% (~99%) between 3.49 and 3.99 MeV (3.99 and 4.49 MeV) and 100% above 4.49 MeV.

B. Water system

To keep the long light attenuation length of the SK water stable, the water is continuously purified with a flow rate of 60 ton/hour. Purified water supplied to the bottom of the detector replaces water drained from its top. A higher temperature of the supply water than the detector temperature

TABLE I. Normal data-taking trigger types along with the threshold of hits and average trigger rates.

Trigger type	Hits in 200 ns	Trigger rate
Super low energy (SLE)	34	3.0–3.4 kHz
Low energy (LE)	47	~40 Hz
High energy (HE)	50	~10 Hz

results in convection throughout the detector volume. This convection transports radioactive radon gas, which is produced by radioactive decays from the U/Th chain near the edge of the detector into the central region of the detector. Radioactivity coming from the decay products of radon gas (most commonly ^{214}Bi beta decays) mimics the lowest energy solar neutrino events. In January of 2010, a new automated temperature control system was installed, allowing for control of the supply water temperature at the ± 0.01 degree level. By controlling the water flow rate and the supply water temperature with such high precision, convection within the tank is kept to a minimum and the background level in the central region has since become significantly lower.

C. Event reconstruction

The methods used for the vertex, direction, and energy reconstructions are the same as those used for SK-III [9]. The Cartesian coordinate system for the SK detector is shown in Fig. 1.

1. Vertex

The vertex reconstruction is a maximum likelihood fit to the arrival times of the Cherenkov light at the PMTs [8]. Figure 2 shows the vertex resolution for each SK phase. The large improvement in SK-III compared to SK-I is the result of using an advanced vertex reconstruction program, while the improved timing resolution and slightly better agreement of the timing residuals between data and Monte Carlo (MC) simulated events are responsible for the additional improvement of SK-IV. We observed a bias in the reconstructed vertex called the vertex shift. This vertex shift is measured with a gamma-ray source at several positions within the SK detector: neutrons from spontaneous fission of ^{252}Cf are thermalized in water and then captured on nickel in a spherical vessel [7,11]. The nickel then emits 9 MeV gammas (Ni calibration source). Figure 3 shows the shift of the reconstructed vertex of these Ni gammas in SK-IV from their true position (assumed to be the source position). The SK-IV vertex shift is improved compared with SK-I, II, and III [7–9].

2. Direction

A maximum likelihood fit comparing the Cherenkov ring pattern of data to MC simulations is used to reconstruct
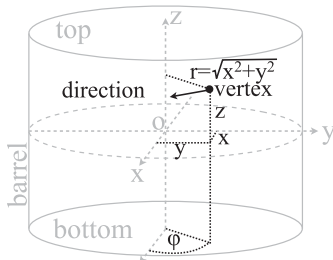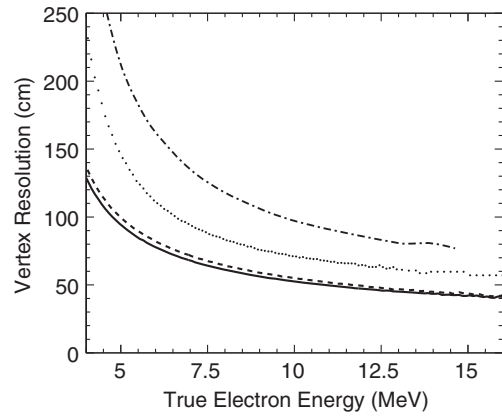

FIG. 2. Vertex resolution for SK-I, II, III, and IV shown by the dotted, dashed-dotted, dashed, and solid lines, respectively. The SK-III vertex resolution improvement over SK-I comes from using an improved vertex reconstruction while the slightly improved timing resolution and better agreement between data and simulated events are responsible for the further improvement in SK-IV.

event directions. During the SK-III phase an energy dependence was included in the likelihood and the angular resolution was improved by about 10% (10 MeV electrons) compared to SK-I. The angular resolution in SK-IV is similar to that in SK-III.

3. Energy

The energy reconstruction is based on the number of PMT hits within a 50 ns time window, after the photon travel time from the vertex is subtracted. This number is then corrected for water transparency, dark noise, late arrival light (due to scattering and reflection), multiphoton hits, etc., producing an effective number of hits N_{eff} (see [9]). Simulations of monoenergetic electrons are used to produce a function relating N_{eff} to the recoil electron energy (MeV).

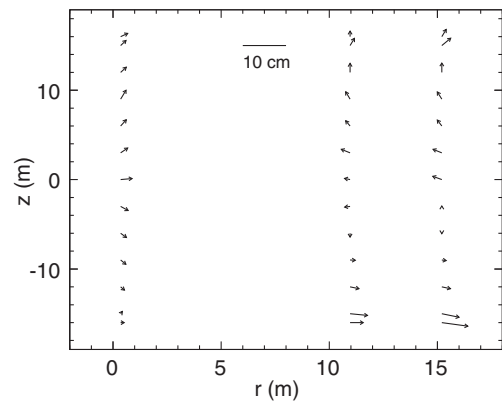FIG. 3. Vertex shift of the Ni calibration events in SK-IV. The start of the arrow is at the true Ni-Cf source position and the direction indicates the averaged vertex shift at that position. The length of the arrow indicates the magnitude of the vertex shift. To make the vertex shifts easier to see this length is scaled up by a factor of 20.

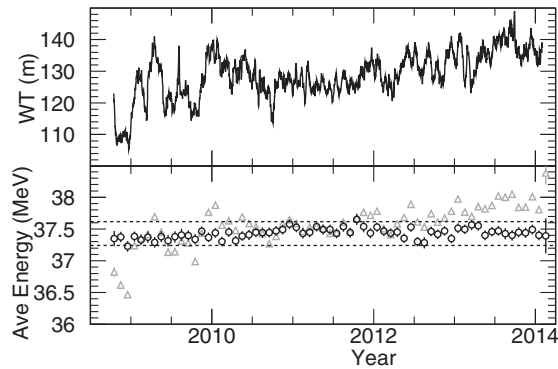FIG. 1. Definition of the SK detector coordinate system.

FIG. 4. Top: Time variation of the water transparency as measured by decay electrons. Bottom: Time variation of the mean reconstructed energy of μ decay electrons before (after) water-transparency correction in triangles (circles). Before the correction, a water transparency of 90 m is assumed, then the mean value of the distribution is adjusted to that of the distribution after the correction. After the correction the mean energy is stable within $\pm 0.5\%$ (dashed lines).

The water transparency parameter used in the energy reconstruction is measured using decay electrons from ray muons. This method of obtaining the water transparency is the same as for SK-I, II, and III [1,8,9]: exploiting the azimuthal symmetry of the Cherenkov cone, we determine the light intensity as a function of light travel distance and fit it with an exponential light attenuation function. The top panel of Fig. 4 shows the time variation of the measured water transparency, while the bottom panel shows the reconstructed mean energy of μ decay electrons in triangles (circles) before (after) water transparency corrections have been applied. The stability of the water transparency corrected energy reconstruction is within $\pm 0.5\%$ (dashed lines).

4. Multiple scattering goodness (MSG)

Even at the low energies of the recoil electrons from ^{8}B solar neutrino-electron scattering, the PMT hit pattern from the Cherenkov cone reflects the amount of multiple Coulomb scattering recoil electrons experience. Very low-energy electrons will incur such scattering more than higher energy electrons and thus have a more isotropic PMT hit pattern. Radioactive background events, such as ^{214}Bi beta decays, generally have less energy than ^{8}B recoil electrons. Radioactive background events with γ emission will be more isotropic still. The "goodness" of a directional fit character-izes this hit pattern anisotropy: it is constructed by first projecting $42°$ cones from the vertex position, centered around each PMT that was hit within a 20 ns time window (after time of flight subtraction). Pairs of such cones are then used to define "event direction candidates," which are vectors along the intersection lines of the two cones. Only cone pairs which intersect twice are used to define event direction candidates. Figure 5 shows a schematic view of how the event direction candidates are found. The gray points represent hit
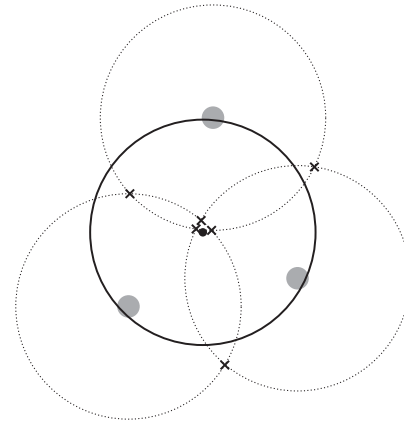

FIG. 5. Schematic view of the event direction candidates used to calculate the multiple scattering goodness. The gray points represent PMT hits and the dotted circles surrounding them are the projections of the $42°$ cones centered around each hit. The black crosses give the intersection points of the cones. The vectors from the event vertex position to these intersection points are taken as event direction candidates. The black dot shows the event best fit direction and the black solid circle is the projection of its Cherenkov cone onto the inner detector wall. The intersections will cluster around the event direction.

PMTs, which will roughly be found around the Cherenkov "ring," the projection of the cone onto the inner detector wall shown by the gray circle. As seen in the figure, for pairs of PMTs with positions located near the Cherenkov ring, one of the intersection lines shown by the black crosses will fall close to the best fit direction vector shown as the black point on the inner detector wall which this vector passes through. Clusters of these event direction candidates are then found by associating other event direction candidates which are within $50°$ of a "central event direction" seeded by the candidates themselves. Once an event direction candidate has been associated to a cluster, it then will not seed another cluster. The event direction candidate vectors of a cluster are added together to adjust the central event direction. Several iter-ations of this adjustment with subsequent cluster reassign-ment will center the clusters and maximize the magnitude of the vector sum. The vector sum with the largest magnitude is kept as the "goodness direction." The multiple scattering goodness (MSG) is then defined by the ratio of this magnitude and the number of event direction candidates within the 20 ns time window. Electrons undergoing more multiple Coulomb scattering will have a lower MSG value than those undergoing less. The filled squares (error bars) and solid (dotted) lines of Fig. 6 compare the LINAC data and MC MSG distributions for 4.38 MeV (8.16 MeV) electrons. As expected, higher energy electrons have a larger mean MSG since they undergo less multiple Coulomb scattering.

D. Energy calibration

The absolute energy scale is determined by an electron linear accelerator (LINAC) [12]. The LINAC calibration
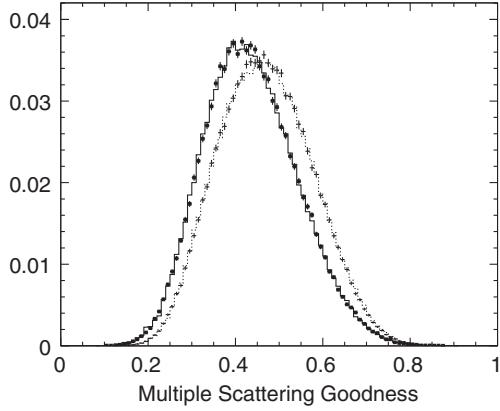
FIG. 6.   MSG for LINAC data (points) and MC (histogram), normalized by the number of events. The solid (dotted) lines and points on that correspond to 4.38 MeV (8.16 MeV) electrons.

FIG. 8.   Difference of the mean reconstructed energy between data and simulated events, at each position, coming from the SK-IV DT calibration.

system injects single monoenergetic electrons into SK in the downward direction. The energy of the momentum-selected electrons is precisely measured by a germanium (Ge) detector using a thin titanium window similar to that used under the water. To determine the energy scale, 6.28 and 12.93 MeV electron data are compared to simulated events. Figure 7 shows the z dependence of this comparison. We cross check the energy scale obtained from the LINAC energy with ^{16}N β/γ decays, which originate from the (n,p) reaction of ^{16}O with neutrons produced by a deuterium-tritium (DT) fusion neutron generator [13]. The 10.5 MeV endpoint ^{16}N decays of the DT calibration are isotropic, with 66% of the decays emitting a 6 MeV γ in conjunction with an electron. DT-produced ^{16}N data are taken at a much larger number of positions in SK than LINAC data. Figure 8 compares the reconstructed energy of ^{16}N simulated events with data, as a function of the z position of the production. The observed dependence on z is probably due to an imperfect model of the z dependence

of the optical parameters (see subsection II E). Figure 9 shows the directional dependence of the energy scale, with respect to the detector zenith angle. The two bins between $\cos\theta_{z_{SK}} = 0.6$ and 1 are affected by increased shadowing from the DT generator. Conservatively, we fit the entire data with a linear combination of a constant and an exponential function to estimate the systematic uncertainty on the day/night asymmetry due to the directional dependence of the bias of the reconstructed energy.

The systematic uncertainty of the energy scale due to position (direction) dependence is estimated to be 0.44% (0.1%). The effect of the water transparency variation during LINAC calibration is estimated to be 0.2%, while the uncertainty of the LINAC electron beam energy (as measured by the Ge detector), is estimated to be 0.21%. The total systematic uncertainty of the absolute energy

FIG. 9.   Difference of the mean energy between data and simulated events as a function of the zenith angle in the SK-IV detector for DT calibration. After subtracting the absolute offset, the uncertainty is estimated to be $\pm 0.1\%$.

FIG. 7.   LINAC calibration z position dependence of the absolute energy scale of SK-IV.

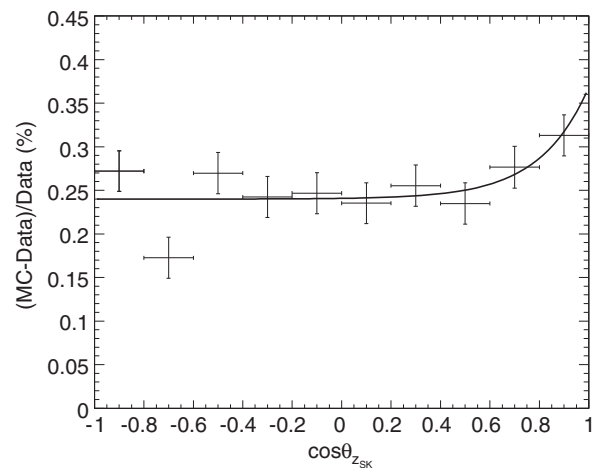scale thus becomes 0.54%, calculated by adding all the contributions in quadrature, and is summarized in Table II. These uncertainties are similar to those in SK-III (0.53%).

The detector's energy resolution is determined using the same method as described in [9]. Monoenergetic electrons are simulated and used to determine the relationship between the effective number of hits in the detector and the electron energy in MeV. Using the width of Gaussian fits to the energy distributions resulting from these simulated electrons, the energy dependence of the energy resolution is well described by the function

$$\sigma(E) = -0.0839 + 0.349\sqrt{E} + 0.0397E, \quad (2.1)$$

in units of MeV, where E is electron total energy. This is comparable to the SK-III energy resolution, given as $\sigma(E) = -0.123 + 0.376\sqrt{E} + 0.0349E$ in [9].

E. Light propagation in water

1. Water parameters

The water transparency in the MC simulation is determined using absorption and scattering coefficients as a function of wavelength (full details of this and other more general detector calibrations can be found in [11]). These coefficients are independently measured by a nitrogen laser and laser diodes at five different wavelengths: 337 nm, 375 nm, 405 nm, 445 nm, and 473 nm. Based on these measurements, the dominant contribution to the variation of the water transparency is a variation in the absorption length. The absorption coefficient is time and position dependent, as explained below. This SK-IV solar neutrino analysis only varies the absorption, and uses a single set of time independent scattering coefficients, as measured by the laser diodes [11].

2. Time dependence

To track the absorption time dependence, we measure the light attenuation of Cherenkov light from decay electrons (from cosmic-ray muons stopping throughout the SK inner detector volume). This measurement uses the azimuthal symmetry of the emitted Cherenkov cone to compare different light propagation path lengths within the same event and assumes a simple exponential attenuation. This effective attenuation length is one of the energy reconstruction parameters. The top panel of Fig. 4 shows

TABLE II. Systematic uncertainty of the energy scale.

Position dependence	0.44%
Direction dependence	0.10%
Water transparency	0.20%
LINAC energy	0.21%
Total	0.54%

the decay electron water transparency parameter as a function of time.

In order to connect the absorption time dependence in the MC to the water transparency parameter measured by decay electrons we generate monoenergetic electron samples throughout the detector for a wide range of absorption coefficients with nine different energies between 4 and 50 MeV. Each MC sample is assigned a particular decay electron water transparency parameter that minimizes the difference between input energy and average reconstructed energy. As expected, the relationship between water transparency and MC absorption coefficient does not significantly depend on the generated energy. The same procedure establishes the relationship between the (corrected) number of PMT hits and energy. Figure 10 shows the obtained relationship between absorption coefficient and water transparency parameter. For convenience we measure the absorption coefficient relative to the coefficient at the time of the LINAC calibration data-taking, which defines the energy scale (see [11]). We employ a linear interpolation between the data points. The mean energy of these decay electrons is used to evaluate the systematic uncertainty of the time dependence of the energy scale (see bottom panel of Fig. 4). After correction for the time variation of the absorption coefficient, the apparent time dependence of the μ decay electron mean energy becomes smaller than $\pm 0.5\%$.

3. Position dependence

As already explained, the water in the SK detector is continuously recirculated through the SK water purification system. Water is drained from the detector top, purified, and reinjected at the bottom. Due to careful temperature control of the injected water, the convection inside the SK tank is suppressed everywhere but at the bottom part of the tank below $z = -11$ m. Figure 11 shows the typical water
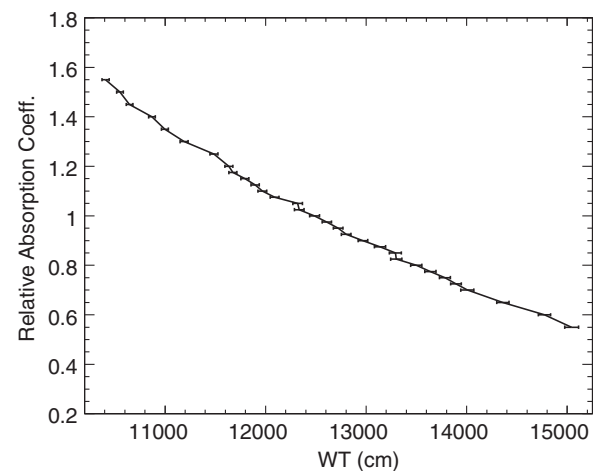

FIG. 10. Change in the absorption coefficient, relative to the coefficient when the absolute energy scale calibration was done, as a function of the μ decay electron measured water transparency.
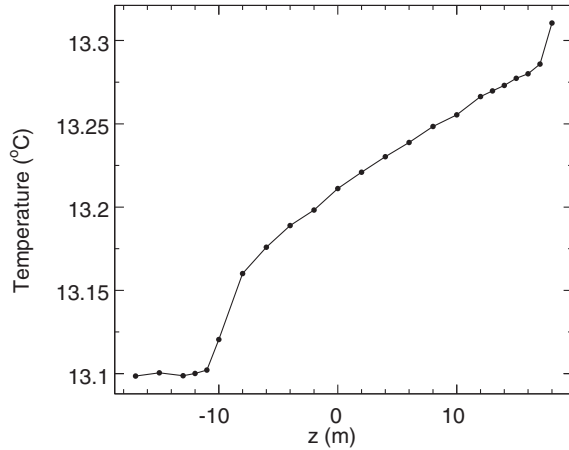
FIG. 11. Typical z dependence of the water temperature in SK detector. Below -11 m the temperature is constant due to convection, and so the absorption coefficient is assumed to be constant below this point.

temperature as a function of z in the SK detector. The temperature is uniform below $z = -11$ m, where convection is occurring and increases steadily above that. We assume that absorption is strongly correlated with the amount of convection and model the position dependence of the absorption length as constant below -11 m and linearly changing above -11 m:

$$
\alpha_{abs}(\lambda, z, t)
$$
$$
= \begin{cases} \alpha(\lambda, t)(1 + \beta(t) \cdot z), & \text{for } z \geq -11 \text{ m} \\ \alpha(\lambda, t)(1 - \beta(t) \cdot 11), & \text{for } z \leq -11 \text{ m,} \end{cases} \quad (2.2)
$$

where β parametrizes the z-dependence of the absorption. The β parameter is determined by studying the distribution of hit PMTs of Ni calibration data (see Sec. II C) [11] in the "top," "bottom," and "barrel" regions of the detector (see Fig. 1). After other detector asymmetries like quantum efficiency variations of the PMTs are taken into account, the hit rate of the top region in the detector is $3 \sim 5\%$ lower than that of the bottom region. β is then fit using the hit asymmetry of Ni calibration events. Since the Ni calibration hit pattern varies with time, both α and β depend on time. The Xe flash lamp scintillator ball calibration system [11] tracks the β time dependence: a Xe flash lamp powers a scintillator ball located near the middle of the detector. The time dependence of β is also monitored by Ni calibration data. The introduction of β into the MC simulation has helped to reduce the systematic uncertainty on the energy scale, as it addresses a significant contribution to its directional dependence. This is important for the solar neutrino day/night asymmetry analysis.

III. DATA ANALYSIS

After installation of the new front-end electronics, SK-IV physics data-taking started on October 6, 2008. This paper

includes data taken from October 6, 2008 until February 1, 2014. The total livetime is 1664 days. The entire data period was taken with a new very low energy threshold of 34 hits within 200 ns (cf. Table I). To reduce the required data storage capacity, obvious backgrounds are removed using faster and less-stringent implementations of the analysis cuts on fiducial volume, energy, ambient events and external events, before the data is permanently stored. By applying these precuts, the data load was reduced to $\sim 1\%$ of its original size.

A. Event selection

Most of the cuts used are the same as those used in SK-III [9], but some of the cut values and the energy regions in which they are applied are changed to optimize the significance: if S (BG) is the number of signal (background) events, we define the significance as $S/\sqrt{BG}$. Also, as was the case in SK-III, below 4.99 MeV the fiducial volume is reduced since backgrounds appear localized at the bottom of the detector and at large radii.

1. Ambient background reduction

As in [1,8,9], several cuts remove low-energy radioactive backgrounds. These backgrounds originate mostly from the PMT enclosures, the PMT glass, and the detector wall structure. While the true vertices lie outside the fiducial volume, some radioactive background events are misreconstructed inside the fiducial volume. The quality of the event reconstruction is tested by variables describing its goodness. The first variable is a timing goodness g_t testing the "narrowness" of the PMT hit timing residuals, which is defined in [8] [Sec. III B, Eq. (3.1)]. The second is a hit pattern goodness g_p testing the azimuthal symmetry of the Cherenkov cone ($g_p = 0$ is perfectly symmetric, $g_p = 1$ is completely asymmetric). Good single electron events must have $g_t^2 - g_p^2$ greater than 0.2. Events below 6.99 MeV (4.99 MeV) must have $g_t^2 - g_p^2$ greater than 0.25 (0.29). The same cut was applied for SK-III.

We also check the consistency of the observed light pattern with a single 42° Cherenkov cone as in [1] [Sec. VII C, Eq. (7.4)]. This cut will remove events with multiple Cherenkov cones, e.g., from beta decays to an excited nuclear state with subsequent gamma emission. The hit pattern is assigned a likelihood based on the direction fit likelihood function. Figure 12 shows the likelihood and cut criteria in three different energy ranges. Further details are found in [14].

A small hit cluster cut targets radioactive background events in the PMT enclosures or glass, which coincide with an upward fluctuation of the PMT dark noise. Only events with a reconstructed r^2 bigger than 155 m^2 (120 m^2), a reconstructed z smaller than -7.5 m (-3 m), or a reconstructed z bigger than 13 m, for reconstructed energies in 4.49–4.99 MeV (3.49–4.49 MeV), are subject to this cut. To characterize small hit clusters, we select PMT hits with
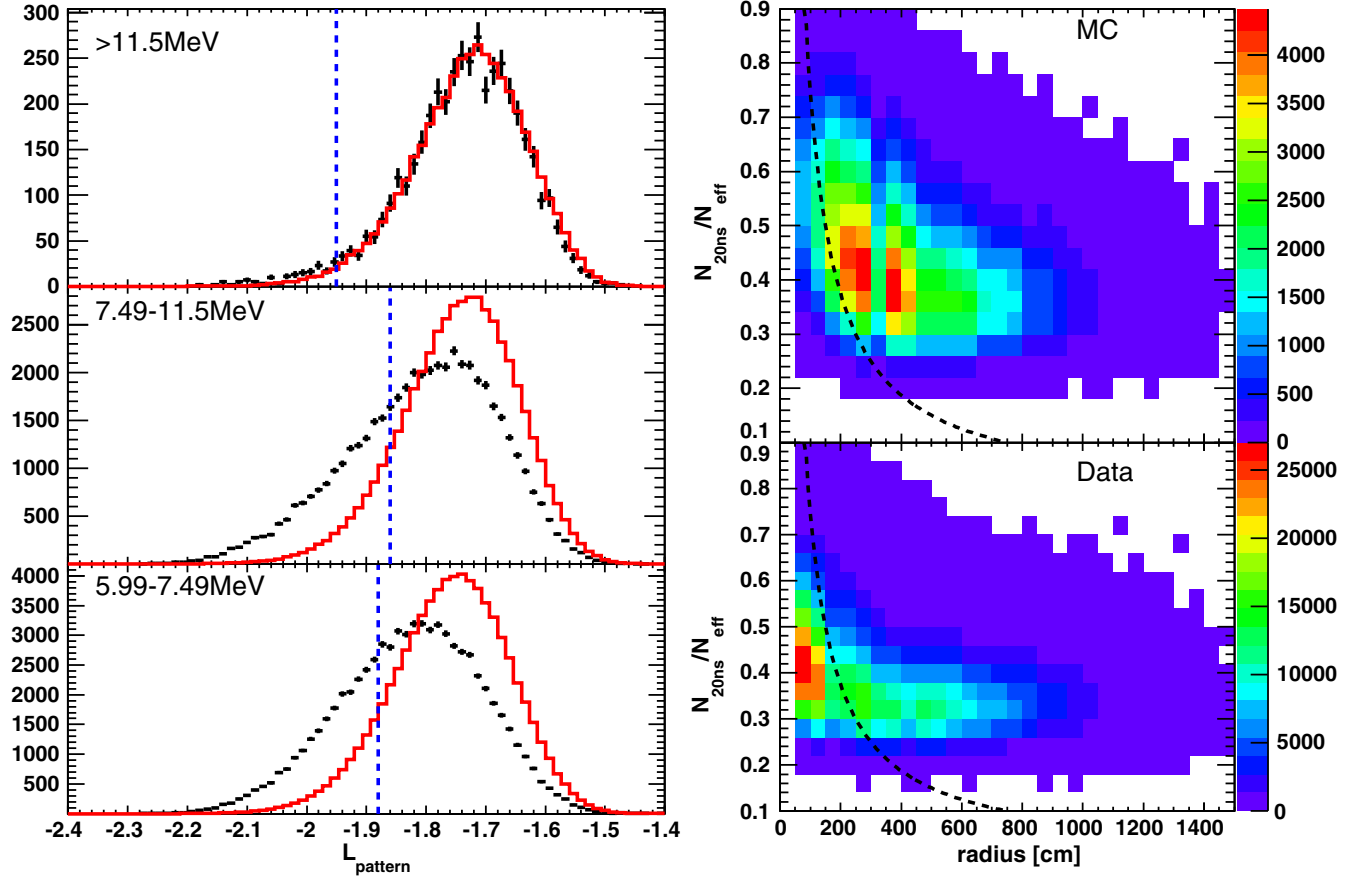
FIG. 12.   Left: Hit pattern likelihood distributions in three different energy ranges for data (black error bars) and MC (red histogram). The cut point is shown by the blue dashed line. Right: Removal of small hit clusters. The top panel shows the MC cluster size vs the cluster radius, the bottom panel is the data. Events below the dashed black line are removed.

times coincident within 20 ns (after time-of-flight subtraction, see Sec. II C 3), and then find the smallest sphere around any of the selected PMTs that encloses at least 20% of all selected PMTs. This radius is multiplied by the ratio of PMT hits coincident within 20 ns (without time-of-flight correction) divided by N_{eff} (see Sec. II C 3). Solar neutrinos near the edge of the fiducial volume have a bigger radius × hit ratio (see also Sec. III C in [9], Fig. 17 and 18) than the radioactive background. As in SK-III, we remove events with radius × hit ratio less than 75 cm as shown in Fig. 12.

Finally, we remove spurious events due to various calibration sources (mostly radioactive decays), if they are below

4.99 MeV. A reconstructed position closer than 2 m to the source, or closer than 1 m to the source or water temperature sensor cable (all cables run along the z axis from the top down to the source position) means the event is removed. The loss in the fiducial volume is about 0.48 kton. Table III lists the various calibration sources which are considered.

2. External event cut

To remove radioactive background coming from the PMTs or the detector wall structure, we calculate the distance to the PMT-bearing surface from the reconstructed vertex looking back along the reconstructed event direction. Radioactive backgrounds tend to appear "incoming," so we remove events where this distance is small. Solar neutrino candidates above 7.49 MeV (above 4.99 MeV and below 7.49 MeV) must have a distance of at least 4 m (6.5 m). In the energy region below 4.99 MeV we distinguish between the "top" (cylinder top lid), "barrel" (cylinder side walls) and "bottom" (cylinder bottom lid) surfaces, shown in Fig. 1. Candidates which come from the "top" ("bottom") must have a distance of at least 10 m (13 m), while "barrel" event candidate distances must exceed 12 m. SK-III applied the same cuts.

TABLE III.   Locations used by the calibration source cut. The sources are described in detail in [11].

Source	x (cm)	y (cm)	z (cm)
Xenon flasher	353.5	−70.7	0.0
LED	35.5	−350.0	150.0
TQ Diffuser Ball	−176.8	−70.7	100.0
DAQ Rate Test Source	−35.3	353.5	100.0
Water Temp. Sensors 1	−35.3	1200	−2000
Water Temp. Sensors 2	70.7	−777.7	−2000

3. Spallation cut

Some cosmic-ray μ's produce radioactive elements by breaking up an oxygen nucleus [15]. A spallation event occurs when these radioactive nuclei eventually decay and emit β's and/or γ's. A spallation likelihood function is made from the distance of closest approach between the preceding μ track(s) and a solar neutrino candidate, their time difference, and the charge deposited by the preceding μ(s). By using the likelihood function spallation-like events are rejected, see [1,16] for details.

When lower energy cosmic-ray μ^-'s are captured by ^{16}O nuclei in the detector, ^{16}N can be produced which decays with gamma-rays and/or electrons with a half-life of 7.13 sec. In order to reject these events, the correlation between stopping μ's in the detector and the remaining candidate events are checked. The cut criteria for ^{16}N events is as follows; (1) reconstructed vertex is within 250 cm to the stopping point of the μ, (2) the time difference is between 100 μ sec and 30 sec.

To measure their impact on the signal efficiency, the spallation and ^{16}N cuts are applied to events that cannot be correlated with cosmic-ray muons (e.g. candidates preceding muons instead of muons preceding candidates). This "random sample" then measures the accidental coincidences rate between the muons and subsequent candidate events. The spallation (^{16}N) cut reduces signal efficiency by about 20% (0.53%).

4. Fiducial volume cut

Events which occur near the wall of the detector (reconstructed within 2 m from the ID edge) are rejected. The volume of this fiducial volume is 22.5 kton. Below 4.99 MeV this cut is tightened. Figure 13 shows the r^2 ($=x^2 + y^2$) vs z data vertex distribution for 3.49 to 3.99 MeV, after the above cuts. Each bin shows the rate (events/day/bin), with blue showing a lower rate and red a

higher rate. We expect solar neutrino events to be uniformly distributed throughout the detector volume, and the regions with high event rates are likely dominated by background. To increase the significance in the final data sample for this energy region (3.49 to 4.49 MeV), we have reduced the fiducial volume to the region shown by the black line in the figure and described by

$$r^2 + \frac{150}{11.75^4} \times |z - 4.25|^4 \leq 150, \qquad (3.1)$$

where the coordinates are given in meters. This function was chosen in order to approximately follow the contours of constant event rate. For the energy range of 4.49 to 4.99 MeV, events which have $r^2 > 180$ m^2 or $z < -7.5$ m are cut.

5. Other cuts

Short runs (<5 minutes), runs with hardware and/or software problems, and calibration runs are not used for this analysis. Cosmic-ray μ events are removed by rejecting events with more than 400 hit PMTs, which corresponds to about 60 MeV for electron type events.

6. Summary

Figure 14 shows the energy spectrum after each reduction step and Fig. 15 shows the reduction efficiency of the corresponding steps. The final sample of SK-IV data is shown by the filled squares and for comparison the SK-III final sample is superimposed (dashed lines). Above 5.99 MeV, the efficiency for solar neutrinos in the final sample is almost the same as in SK-III, while for 4.99 to 5.99 MeV, the SK-IV efficiency is better than SK-III. The reason for the improvement is the removal of a fiducial
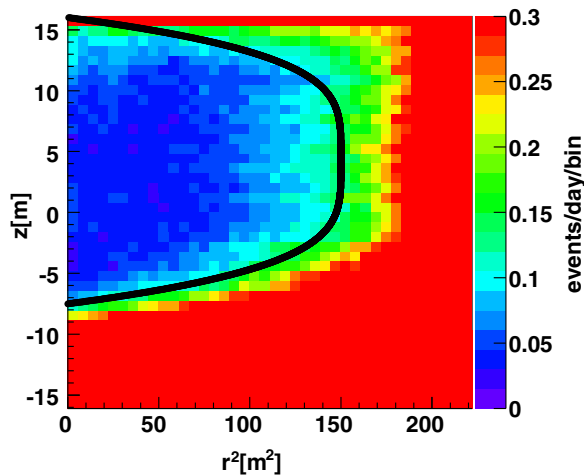

FIG. 13. Vertex distribution for 3.49 to 3.99 MeV data. Radioactive background leads to a large event rate at the bottom and large radii. The black line indicates the reduced fiducial volume in this energy region.

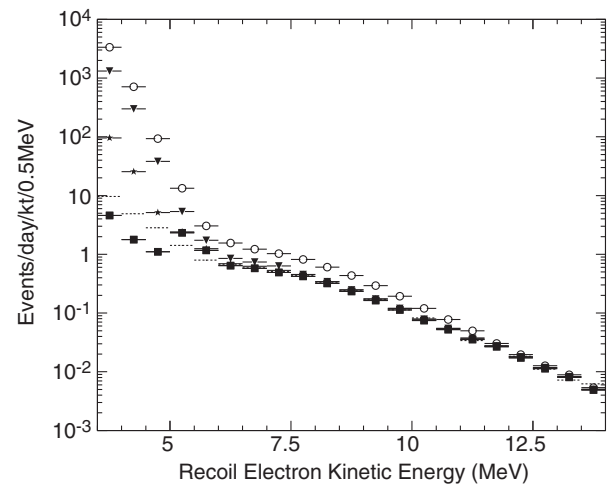FIG. 14. Energy spectrum after each reduction step in the 22.5 kton fiducial volume. The open circles (filled inverted triangles) correspond to the reduction step after the spallation (ambient) cut. The stars give the spectrum after the external event cut, and the final SK-IV sample after the tight fiducial volume cut is given by the filled squares. The dashed line shows the final sample of SK-III.
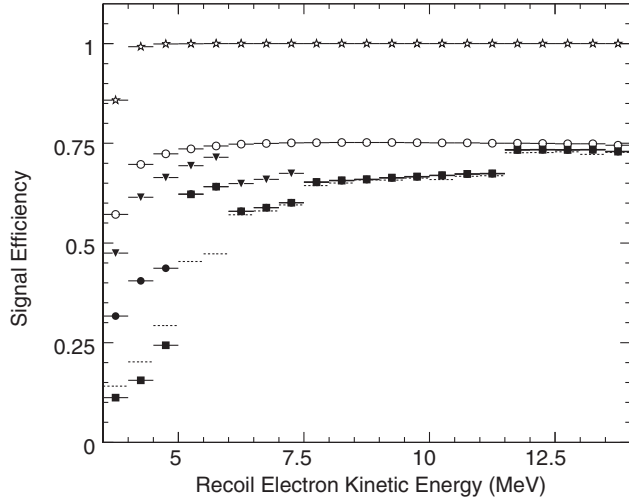
FIG. 15. Signal efficiency after each reduction step. The open stars are the trigger efficiency in the 22.5 kton fiducial volume, the open circles (filled inverted triangles) correspond to the reduction step after the spallation (ambient) cut. The filled squares give the final reduction efficiency, with the step from the filled circles (after the external event cut) to the filled squares indicates the reduction in fiducial volume at low energy. The dashed line shows the efficiency of SK-III.

volume cut based on the "second vertex fit" [1,9] and making a looser ambient event cut. The reduced fiducial volume and a tighter ambient event cut for 3.49 to 4.99 MeV results in a lower efficiency than SK-III, but in exchange the background level has been reduced by ~40%.

B. Simulation of solar neutrinos

There are several steps in simulating solar neutrino events at SK: generate the solar neutrino fluxes and cross sections, determine the recoil electron kinematics, track the Cherenkov light in water and simulate the response of the PMTs and electronics. We used the ^{8}B solar neutrino spectrum calculated by Winter *et al.* [17] and the *hep* solar neutrino spectrum. The systematic uncertainties from these flux calculations are incorporated in the energy-correlated systematic uncertainty of the recoil electron spectrum. The simulated event times are chosen according to the livetime distribution of SK-IV so that the solar zenith angle distribution of the solar neutrinos is reflected correctly across the simulated events. The recoil electron energy spectrum is calculated by integrating the differential cross section between zero and T_{max}. T_{max} is the maximum kinetic energy of the recoiling electron, which is limited by the incident neutrino energy.

Because ν_e's scatter via both $W^{\pm}$ and Z^0 exchange, while $\nu_{\mu,\tau}$'s interact only in the neutral-current channel, the (ν_e, e^-) cross section is approximately six times larger than $(\nu_{\mu,\tau}, e^-)$. For the total and differential cross sections of those interactions, we adopted the calculation from [18], in which the radiative corrections are taken into account and
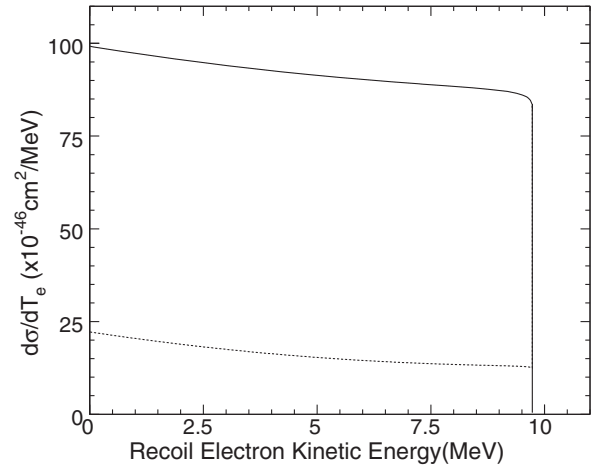

FIG. 16. Differential cross section of (ν_e, e) (solid) and $(\nu_{\mu,\tau}, e)$ (dashed) elastic scattering for the case of 10 MeV incident neutrino energy.

where the ratio $d\sigma_{\nu_e}/dE_e$ and $d\sigma_{\nu_{\mu,\tau}}/dE_e$ depends on the recoil electron energy E_e. Figure 16 shows the differential cross section of (ν_e, e^-) (solid) and $(\nu_{\mu,\tau}, e^-)$ (dashed) elastic scattering, for the case of 10 MeV incident neutrino energy. This recoil electron energy dependence of the cross section was accidentally omitted in the SK-III flux calculation in [9]. Therefore, wrong recoil electron kinematics were generated for the SK-III analysis, primarily affecting the lowest energy. We reanalyzed SK-III with the correct energy dependence (leaving everything else unchanged), the results of which can be found in Appendix A.

C. Total flux

In the case of (ν, e^-) interactions of solar neutrinos in SK, the incident neutrino and recoil electron directions are highly correlated. Figure 17 shows the $\cos\theta_{sun}$ distribution for events in the energy range 3.49 to 19.5 MeV, as well as the definition of $\cos\theta_{sun}$. In order to obtain the number of solar neutrino interactions, an extended maximum likelihood fit is used. This method is also used in the SK-I [1], II [8], and III [9] analyses. The likelihood function is defined as

$$\mathcal{L} = e^{-(\sum_i B_i + S)} \prod_{i=1}^{N_{bin}} \prod_{j=1}^{n_i} (B_i \cdot b_{ij} + S \cdot Y_i \cdot s_{ij}), \quad (3.2)$$

where N_{bin} is the number of energy bins. The flux analysis of SK-IV has $N_{bin} = 23$ energy bins; 20 bins of 0.5 MeV width between 3.49 and 13.5 MeV, two energy bins of 1 MeV between 13.5 MeV and 15.5 MeV, and one bin between 15.5 MeV and 19.5 MeV. n_i is the number of observed events in the ith energy bin. S and B_i, the free parameters of this likelihood function, are the number of solar neutrino interactions in all bins and the number of background events in the ith energy bin, respectively. Y_i is the fraction of signal events in the ith energy bin, calculated from solar neutrino simulated events. The background weights
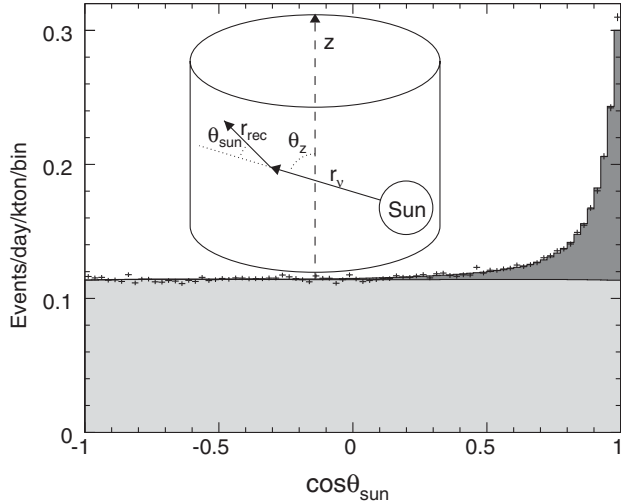
FIG. 17.   Solar angle distribution for 3.49 to 19.5 MeV. θ_{sun} is the angle between the incoming neutrino direction r_ν and the reconstructed recoil electron direction r_{rec}. θ_z is the solar zenith angle. Black points are data while the histogram is the best fit to the data. The dark (light) shaded region is the solar neutrino signal (background) component of this fit.

$b_{ij} = \beta_i(\cos\theta_{ij}^{\mathrm{sun}})$ and the signal weights $s_{ij} = \sigma(\cos\theta_{ij}^{\mathrm{sun}}, E_{ij})$ are calculated from the expected shapes of the background and solar neutrino signal, respectively (probability density functions). The background shapes β_i are based on the zenith and azimuthal angular distributions of real data, while the signal shapes σ are obtained from the solar neutrino simulated events. The values of S and B_i are obtained by maximizing the likelihood. The histogram of Fig. 17 is the best fit to the data, the dark (light) shaded region is the solar neutrino signal (background) component of that best fit. The systematic uncertainty for this method of signal extraction is estimated to be 0.7%.

1. Vertex shift systematic uncertainty

The systematic uncertainty resulting from the fiducial volume cut comes from event vertex shifts. To calculate the effect on the elastic scattering rate, the reconstructed vertex positions of solar neutrino MC events are artificially shifted following the arrows in Fig. 3, and the number of events passing the fiducial volume cut with and without the artificial shift are compared. Figure 18 shows the energy dependence of the systematic uncertainty coming from the shifting of the vertices. The increase below 4.99 MeV comes from the reduced fiducial volume (smaller surface to volume ratio), not from an energy dependence of the vertex shift. The systematic uncertainty on the total rate is ±0.2%.

2. Trigger efficiency systematic uncertainty

The trigger efficiency depends on the vertex position, water transparency, number of hit PMTs, and response of the front-end electronics. The systematic uncertainty
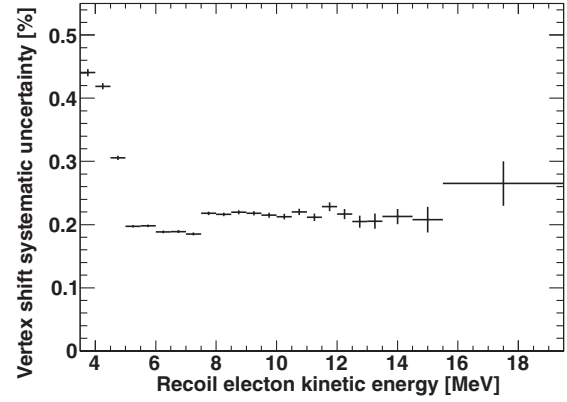
FIG. 18.   Vertex shift systematic uncertainty on the flux. The increase below 4.99 MeV comes from the tight fiducial volume cut. (see text).

from the trigger efficiency is estimated by comparing Ni-calibration data (see Sec. II C) with MC simulation. For 3.49–3.99 MeV and 3.99–4.49 MeV, the difference between data and MC is $-3.43 \pm 0.37\%$ and $-0.86 \pm 0.31\%$, respectively [14]. Above 4.49 MeV the trigger efficiency is 100% and its uncertainty is negligible. The resulting total flux systematic uncertainty due to the trigger efficiency is ±0.1%.

3. Angular resolution systematic uncertainty

The angular resolution of electrons is defined as the angle which includes 68% of events in the distribution of the angular difference between their reconstructed direction and their true direction. The MC prediction of the angular resolution is checked and the systematic uncertainty is estimated by comparing the difference in the reconstructed and true directions of LINAC data and LINAC (see [12]) simulated events. This difference is shown in Table IV for various energies. To estimate the systematic uncertainty on the total flux, the signal shapes $s_{ij}^{\mathrm{ang}+}$ and $s_{ij}^{\mathrm{ang}-}$ are varied by shifting the reconstructed directions of the simulated solar neutrino events by the uncertainty in the angular resolution. These new signal shapes are used when extracting the total

TABLE IV.   Angular resolution difference between LINAC data and simulated LINAC events for each SK phase. The energy refers to the electron's in-tank kinetic energy.

Energy (MeV)	SK-I(%)	SK-II(%)	SK-III(%)	SK-IV(%)
4.0	⋯	⋯	⋯	0.64
4.4	−1.64	⋯	0.74	0.68
5.3	−1.38	⋯	⋯	⋯
6.3	2.32	5.93	⋯	0.02
8.2	2.33	7.10	0.40	0.06
10.3	1.52	⋯	⋯	⋯
12.9	1.07	6.50	−0.27	0.22
15.6	0.88	⋯	0.39	⋯
18.2	⋯	⋯	⋯	0.31

flux, and the resulting $\pm 0.1\%$ change in the extracted flux is taken as the systematic uncertainty from angular resolution.

4. Result

The systematic uncertainty on the total flux (between 3.49 and 19.5 MeV) is summarized in Table V. The energy scale dominates the total systematic uncertainty which is calculated as the quadratic sum of all components, and found to be 1.7%. This is the smallest systematic uncertainty of all phases of SK. In particular, the systematic uncertainties that are energy-correlated (arising from the energy scale and resolution uncertainty) are smallest: while SK-IV's livetime is the same for all energy bins, previous phases have less livetime below 5.99 MeV recoil electron kinetic energy. For example, SK-III data below 5.99 MeV has only about half the livetime as the full SK-III phase. The improved livetime below 5.99 MeV, a higher efficiency in that energy region, and the additional data below 4.49 MeV all lessen the impact of energy scale and resolution uncertainties on the flux determination compared to previous phases. Other contributions to the reduction come from the removal of the fiducial volume cut based on an alternate vertex fit, and better control of vertex shift, trigger efficiency and angular resolution systematic effects. The number of solar neutrino events (3.49–19.5 MeV) extracted from Fig. 17 is $31,891^{+283}_{-281}(\text{stat}) \pm 543(\text{syst})$. This number corresponds to a ^{8}B solar neutrino flux of

TABLE V. Summary of the systematic uncertainty on the total rate for each SK phase. The details are also explained in [9,14].

	SK-I	SK-II	SK-III	SK-IV
Threshold (MeV)	4.49	6.49	3.99	3.49
Trigger efficiency	0.4%	0.5%	0.5%	0.1%
Angular resolution	1.2%	3.0%	0.7%	0.1%
Reconstruction goodness	$^{+1.9}_{-1.3}\%$	3.0%	0.4%	0.1%
Hit pattern	0.8%	$\cdots$	0.3%	0.5%
Small hit cluster	$\cdots$	$\cdots$	0.5%	$^{+0.5}_{-0.4}\%$
External event cut	0.5%	1.0%	0.3%	0.1%
Vertex shift	1.3%	1.1%	0.5%	0.2%
Second vertex fit	0.5%	1.0%	0.5%	$\cdots$
Background shape	0.1%	0.4%	0.1%	0.1%
Multiple scattering goodness	$\cdots$	0.4%	0.4%	0.4%
Livetime	0.1%	0.1%	0.1%	0.1%
Spallation cut	0.2%	0.4%	0.2%	0.2%
Signal extraction	0.7%	0.7%	0.7%	0.7%
Cross section	0.5%	0.5%	0.5%	0.5%
Subtotal	2.8%	4.8%	1.6%	1.2%
Energy scale	1.6%	$^{+4.2}_{-3.9}\%$	1.2%	$^{+1.1}_{-1.2}\%$
Energy resolution	0.3%	0.3%	0.2%	$^{+0.3}_{-0.2}\%$
^{8}B spectrum	$^{+1.1}_{-1.0}\%$	1.9%	$^{+0.3}_{-0.4}\%$	$^{+0.4}_{-0.3}\%$
Total	$^{+3.5}_{-3.2}\%$	$^{+6.7}_{-6.4}\%$	2.2%	1.7%

TABLE VI. SK measured solar neutrino flux by phase.

	Flux ($\times 10^6/(\text{cm}^2 \text{ sec})$)
SK-I	$2.380 \pm 0.024^{+0.084}_{-0.076}$
SK-II	$2.41 \pm 0.05^{+0.16}_{-0.15}$
SK-III	$2.404 \pm 0.039 \pm 0.053$
SK-IV	$2.308 \pm 0.020^{+0.039}_{-0.040}$
Combined	$2.345 \pm 0.014 \pm 0.036$

$$\Phi_{^8\text{B}}(\text{SK} - \text{IV})$$
$$= (2.308 \pm 0.020(\text{stat})^{+0.039}_{-0.040}(\text{syst})) \times 10^6/(\text{cm}^2 \text{ sec}),$$

assuming a pure ν_e flavor content.

As seen in Table VI, the SK-IV measured flux agrees with that of previous phases within systematic uncertainty. It can then be combined with the previous three SK flux measurements to give the SK measured flux as

$$\Phi_{^8\text{B}}(\text{SK})$$
$$= (2.345 \pm 0.014(\text{stat}) \pm 0.036(\text{syst}))$$
$$\times 10^6/(\text{cm}^2 \text{ sec}).$$

IV. ENERGY SPECTRUM

Present values of Δm^2_{21} and $\sin^2\theta_{12}$ imply that solar neutrino flavor oscillations above about three MeV are dominated by the solar MSW [4] resonance, while low-energy solar neutrino flavor changes are mostly due to vacuum oscillations. Since the MSW effect rests solely on standard weak interactions, it is rather interesting to compare the expected resonance curve with data as any deviation would imply new (weak interaction) physics. Unfortunately multiple Coulomb scattering prevents the kinematic reconstruction of the neutrino energy in neutrino-electron elastic scattering interactions. However, the energy of the recoiling electron still provides a lower limit to the neutrino's energy. Thus, the neutrino spectrum is inferred statistically from the recoil electron spectrum. Moreover, the differential cross section of $\nu_{\mu,\tau}$'s is not just a factor of about six smaller than the one for ν_e's, but also has a softer energy dependence. In this way, the observed recoil electron spectrum shape depends both on the flavor composition and the energy dependence of the composition of the solar neutrinos (see Sec. III B in particular Fig. 16). Thus, even a flat composition of 33% ν_e and 67% $\nu_{\mu,\tau}$ would still distort the recoil electron spectrum compared to one with 100% ν_e. The energy dependence of the day/night effect and rare *hep* neutrino interactions (with a higher endpoint than ^{8}B ν's) also distort the spectrum.

Since the transition between MSW resonance and vacuum oscillations lies around 3 MeV, the lowest energy

solar neutrinos show the largest deviation from the reso-nance electron survival probability. Here, we report for the first time, a clear solar neutrino signal with high statistics in the energy range 3.49–3.99 MeV observed over the entire data-taking period of SK-IV. Figure 19 shows the solar angle distribution for this energy bin, with a distinct peak (above the background) coming from solar neutrinos. The number of solar neutrino interactions (measured in this energy range from fits to the distributions of Fig. 20 discussed below) is

$$1063^{+124}_{-122}(\text{stat})^{+55}_{-54}(\text{syst}) \text{ events.}$$

A. SK-IV spectrum results

As outlined in Sec. III C [in particular Eq. (3.2)], the solar neutrino signal of SK-IV is extracted by an extended maximum likelihood fit. While the ^{8}B flux analysis uses all 23 energy bins at once (and constrains the energy spectrum to the one expected from unoscillated simulation via the Y_i factors), *here* we extract the solar neutrino energy spectrum by fitting one recoil electron energy bin i at a time, with $Y_i = 1$. Below 7.49 MeV, each energy bin is split into three subsamples according to the MSG of the events, with boundaries set at MSG = 0.35 and 0.45. These three subsamples are then fit simultaneously to a single signal and three independent background components. The signal fraction Y_{ig} in each MSG bin g is determined by solar neutrino simulated events in the same manner as the Y_i factors in the ^{8}B flux analysis. Similar to the ^{8}B flux analysis, the signal and background shapes depend on the MSG bin g: the signal shapes σ_g are calculated from solar neutrino simulated events and the background shapes β_{ig} are taken from data. Figure 20 shows the measured angular

FIG. 20. Solar angle distribution for the electron energy ranges 3.49–3.99 MeV, 3.99–4.49 MeV, 4.49–4.99 MeV and 6.99–7.49 MeV (from top to bottom), for each MSG bin (left to right). The style definitions are same as Fig. 17.

distributions (as well as the fits) for the energy ranges 3.49–3.99 MeV, 3.99–4.49 MeV, 4.49–4.99 MeV, and 6.99–7.49 MeV (from top to bottom), for each MSG bin (left to right). As expected in the lowest energy bins, where the dominant part of the background is due to very low-energy β/γ decays, the background component is largest in the lowest MSG subsample. Also as expected, the solar neutrino elastic scattering peak sharpens as MSG is increased.

FIG. 19. Solar angle distribution for events with electron energies between 3.49 and 3.99 MeV. The style definitions are same as Fig. 17.

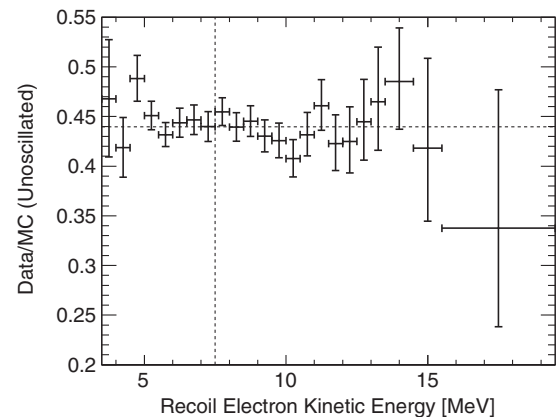FIG. 21. SK-IV energy spectrum using MSG sub-samples below 7.49 MeV, shown as the ratio of the measured rate to the simulated unoscillated rate. The horizontal dashed line gives the SK-IV total average (0.440). Error bars shown are statistical plus energy-uncorrelated systematic uncertainties.
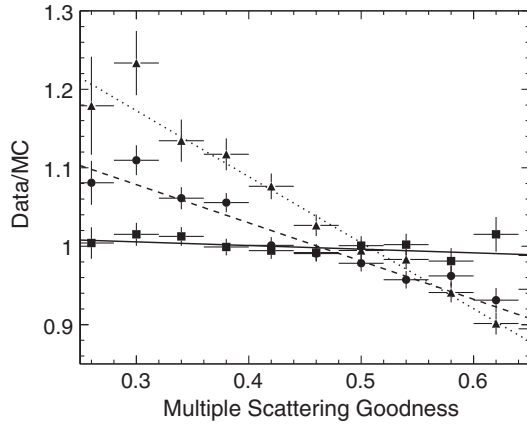
FIG. 22. MSG scaling functions applied to simulated events to estimate the systematic uncertainty on the energy spectrum. The dotted, dashed and solid lines correspond to 16.1, 8.67, and 4.89 MeV LINAC data over simulated events.

Using this method for recoil electron energy bins below 7.49 MeV gives ∼10% improvement in the statistical uncertainty on the number of extracted signal events (the additional systematic uncertainty is small compared to the statistical gain). Figure 21 shows the resulting SK-IV energy spectrum, where below 7.49 MeV MSG has been used and above 7.49 MeV the standard signal extraction method without MSG is used. Table XVI in Appendix B gives the measured and expected rate in each energy bin, as well as that measured for the day and night times separately, along with the 1σ statistical deviations. We reanalyzed the SK-III spectrum below 7.49 MeV with the same method, the same MSG bins and the same energy bins as SK-IV, down to 3.99 MeV. We also refit the entire SK-II (which has poorer resolution) spectrum using the same three MSG sub-samples. The gains in precision are similar to SK-IV. The SK-II and III spectra are given in Sec. IV C.

To analyze the spectrum, we simultaneously fit the SK-I, II, III and IV spectra to their predictions, while varying the

^{8}B and *hep* neutrino fluxes within uncertainties. The ^{8}B flux is constrained to $(5.25 \pm 0.20) \times 10^6/(\text{cm}^2 \text{ sec})$ and the *hep* flux to $(8 \pm 16) \times 10^3/(\text{cm}^2 \text{ sec})$ (motivated by SNO's measurement [19] and limit [20]). The χ^2 is described in detail in Sec. VI.

B. Systematic uncertainties on the energy spectrum

Since we simultaneously fit multiple samples defined by the multiple Coulomb scattering goodness in the lowest recoil electron energy region, a systematic shift in this goodness of the data compared to solar ^{8}B (or *hep*) neutrino simulated events would affect the measured event rate in that energy region. To estimate the systematic effect of using MSG sub-samples, MSG distributions of LINAC data and simulated LINAC events were compared, as seen in Fig. 6. The simulated solar neutrino MSG distributions are adjusted using the observed ratio of the LINAC data and simulated events at the nearest LINAC energy. This changes the solar signal shapes σ_g and the ratios of expected signal events Y_{ig} for MSG bin g. The $\cos\theta_{\text{sun}}$ distributions are then refit, using the new angular distributions and signal ratios and the change in the extracted number of signal events is taken as the systematic uncertainty. The scaling functions for three LINAC energies can be seen in Fig. 22.

The change for each energy bin and all other energy-uncorrelated systematic uncertainties of the SK-IV recoil electron energy spectrum are summarized in Table VII. The total energy-uncorrelated systematic uncertainty in this table is calculated as the sum in quadrature of each of the components. Since we assume no correlations between the energy bins in the SK-IV spectrum analysis, the combined uncertainty is added in quadrature to the statistical error of that energy bin.

The ^{8}B neutrino spectrum uncertainty (a shift of $\sim \pm 100$ keV), the SK-IV energy scale uncertainty ($\pm0.54\%$) and the SK-IV energy resolution uncertainty ($\pm1.0\%$ for < 4.89 MeV, 0.6% for > 6.81 MeV) [14], will

TABLE VII. Energy-uncorrelated systematic uncertainties on the spectrum shape. The systematic error of the (unlisted) small hit cluster cut (only applied below 4.99 MeV) is negligible.

Energy (MeV)	3.49–3.99	3.99–4.49	4.49–4.99	4.99–5.49	5.49–5.99	5.99–6.49	6.49–6.99	6.99–7.49	7.49–19.5
Trigger efficiency	$^{+3.6}_{-3.3}\%$	$\pm0.8\%$	$\cdots$	$\cdots$	$\cdots$	$\cdots$	$\cdots$	$\cdots$	$\cdots$
Reconstruction goodness	$\pm0.6\%$	$\pm0.7\%$	$^{+0.6}_{-0.5}\%$	$\pm0.4\%$	$\pm0.2\%$	$\pm0.1\%$	$\pm0.1\%$	$\pm0.1\%$	$\pm0.1\%$
Hit pattern	$\cdots$	$\cdots$	$\cdots$	$\cdots$	$\cdots$	$\pm0.6\%$	$\pm0.6\%$	$\pm0.6\%$	$\pm0.4\%$
External event cut	$\pm0.1\%$	$\pm0.1\%$	$\pm0.1\%$	$\pm0.1\%$	$\pm0.1\%$	$\pm0.1\%$	$\pm0.1\%$	$\pm0.1\%$	$\pm0.1\%$
Vertex shift	$\pm0.4\%$	$\pm0.4\%$	$\pm0.2\%$	$\pm0.2\%$	$\pm0.2\%$	$\pm0.2\%$	$\pm0.2\%$	$\pm0.2\%$	$\pm0.2\%$
Background shape	$\pm2.9\%$	$\pm1.0\%$	$\pm0.8\%$	$\pm0.2\%$	$\pm0.1\%$	$\pm0.1\%$	$\pm0.1\%$	$\pm0.1\%$	$\pm0.1\%$
Signal extraction	$\pm2.1\%$	$\pm2.1\%$	$\pm2.1\%$	$\pm0.7\%$	$\pm0.7\%$	$\pm0.7\%$	$\pm0.7\%$	$\pm0.7\%$	$\pm0.7\%$
Cross section	$\pm0.2\%$	$\pm0.2\%$	$\pm0.2\%$	$\pm0.2\%$	$\pm0.2\%$	$\pm0.2\%$	$\pm0.2\%$	$\pm0.2\%$	$\pm0.2\%$
MSG	$\pm0.4\%$	$\pm0.4\%$	$\pm0.3\%$	$\pm0.3\%$	$\pm0.3\%$	$\pm1.7\%$	$\pm1.7\%$	$\pm1.7\%$	$\cdots$
Total	$^{+5.1}_{-4.9}\%$	$\pm2.6\%$	$^{+2.4}_{-2.3}\%$	$\pm0.9\%$	$\pm0.9\%$	$\pm2.0\%$	$^{+2.0}_{-1.9}\%$	$\pm1.9\%$	$^{+0.9}_{-0.8}\%$

shift all energy bins in a correlated manner. The size and correlation of these uncertainties are calculated from the neutrino spectrum, the differential cross section, the energy resolution function, and the size of the systematic shifts. We vary each of these three parameters (^{8}B neutrino spectrum shift, energy scale, and energy resolution) individually. Figure 23 shows the result of this calculation. When we analyze the spectrum, we apply these shifts to the spectral predictions. When the SK-IV spectrum is combined with the SK-I, II, and III spectra, the ^{8}B neutrino spectrum shift is common to all four phases, while each phase varies its energy scale and resolution individually (without correlation between the phases).

C. SK-I/II/III/IV combined spectrum analysis

In order to discuss the energy dependence of the solar neutrino flavor composition in a general way, SNO [19] has parametrized the electron survival probability P_{ee} using a quadratic function centered at 10 MeV:

$$P_{ee}(E_\nu) = c_0 + c_1 \left(\frac{E_\nu}{\text{MeV}} - 10 \right) + c_2 \left(\frac{E_\nu}{\text{MeV}} - 10 \right)^2,$$
(4.1)

where c_0, c_1, and c_2 are polynomial parameters.

As seen in Fig. 24, this parametrization does not describe well the MSW resonance based on the oscillation parameters of either best fit. This is also true for alternative solutions such as nonstandard interactions [5] and mass-varying neutrinos [6]. However, it is simple, and the SNO collaboration found that it introduces no

FIG. 24. ν_e survival probability P_{ee} based on the oscillation parameters fit to SK (thick solid green) and all solar neutrino and KamLAND data (thick solid blue). The solid yellow (cyan) line is the best exponential approximation to the thick solid green (blue) line. The dashed black (dotted green) line is the best quadratic (cubic) approximation to the thick solid green line and the dashed red (dotted pink) line the best quadratic (cubic) approximation to the thick solid blue.

bias when determining oscillations parameters. In addition to this quadratic function we have explored two different alternatives to parametrize the survival probability in order to study any limitations the quadratic function might have: an exponential fit and a cubic extension of the quadratic fit. The exponential fit is parametrized as

$$P_{ee}(E_\nu) = e_0 + \frac{e_1}{e_2} \left(e^{e_2 \left(\frac{E_\nu}{\text{MeV}} - 10 \right)} - 1 \right).$$
(4.2)

This particular functional form allows direct comparison of e_0 and e_1 to the quadratic coefficients c_0 and c_1, if c_1 and e_1 are small. The parameter e_2 controls the "steepness" of the exponential fall or rise. Both exponential and cubic parametrizations describe the MSW resonance curve reasonably well as shown in Fig. 24. This is true for both the SK-only and the solar + KamLAND best-fit oscillation parameters discussed in the oscillation section below. Table VIII lists the exponential and cubic coefficients that best describe those two MSW resonance curves. The definition of the spectrum χ^2 and the best-fit values are given in Sec. VI.

To ease the comparison between SK spectral data and SNO's results, we also performed a quadratic fit to SK data. Table IX gives the best quadratic coefficients for both the SK-only and the solar + KamLAND case.
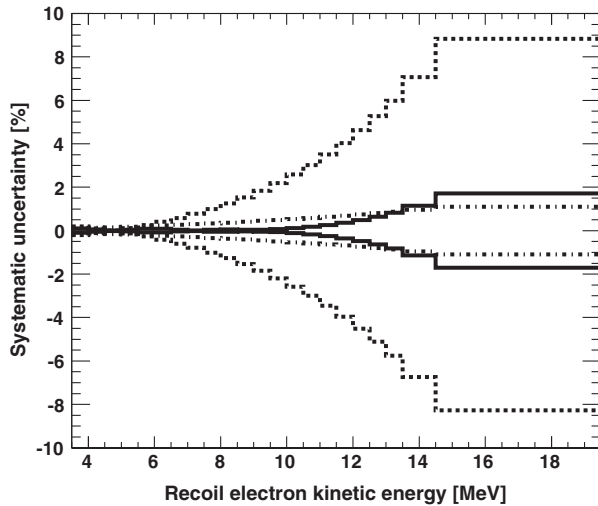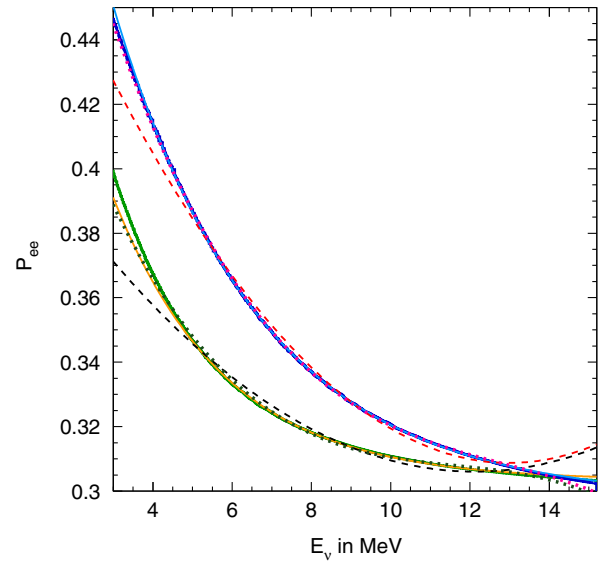

FIG. 23. Energy-correlated systematic uncertainties. The dot-dashed, solid, and dashed distributions correspond to the systematic uncertainties of the ^{8}B spectrum shape, energy resolution, and absolute energy scale, respectively.

TABLE VIII. Best approximations to the MSW resonances using exponential and polynomial parametrizations of P_{ee}.

	$\sin^2\theta_{12} = 0.304$ $\Delta m^2_{21} = 7.41 \times 10^{-5}$		$\sin^2\theta_{12} = 0.314$ $\Delta m^2_{21} = 4.90 \times 10^{-5}$	
Exponential e_0	0.3205		0.3106	
Exponential e_1	−0.0062		−0.0026	
Exponential e_2	−0.2707		−0.3549	
Exponential χ^2	70.69		68.99	
Exponential $\Delta\chi^2$	2.31		0.61	
Polynomial c_0	0.3194	0.3204	0.3095	0.3105
Polynomial c_1	−0.0071	−0.0059	−0.0033	−0.0021
Polynomial c_2	+0.0012	+0.0009	+0.0008	+0.0005
Polynomial c_3	0	−0.0001	0	−0.0001
Polynomial χ^2	70.79	70.71	68.87	69.06
Polynomial $\Delta\chi^2$	2.46	7.07	0.54	5.43

For each set of parameters, the expected rate in each energy bin is adjusted according to the average day/night enhancement expected from $\sin^2\theta_{12} = 0.304$ and $\Delta m^2 = 4.90 \times 10^{-5}$ eV^2. Figure 25 shows the SK spectral data. They are expressed as the ratio of the observed elastic scattering rates of each SK phase over MC expectations, assuming no oscillations (pure electron flavor composition), a ^{8}B flux of $5.25 \times 10^6/(\text{cm}^2 \text{ sec})$ and a *hep* flux of $8 \times 10^3/(\text{cm}^2 \text{ sec})$. Table XVII in Appendix B lists the data shown in Fig. 25, with the given errors including statistical uncertainties as well as energy-uncorrelated systematic uncertainties.

Table XV in Appendix B gives the SK exponential and polynomial best-fit coefficients and their correlations. We compare the best χ^2 of the full MSW calculation to that of the best exponential, cubic, and quadratic function fits, as well as a simple energy-independent suppression of the elastic scattering rate in SK. In the case of the flat (energy-independent) suppression, 0.4268 was chosen as the ratio of observed elastic scattering over expectation assuming no neutrino oscillations. The value 0.4268 corresponds to a constant $P_{ee} = 0.317$ if the cross section ratio was

$d\sigma_{\nu_\mu}/d\sigma_{\nu_e} = 0.16$ independent of energy. In reality, that ratio becomes larger at lower energy, leading to a small low-energy "upturn" even for a constant $P_{ee} = 0.317$. The energy dependence of the day/night effect (which is corrected for in the polynomial and exponential fits) leads to a small "downturn." In case of this flat suppression we fit with and without the day/night correction. Tables IX and X compare the various χ^2, while Table VIII gives the χ^2 from the best exponential (quadratic, cubic) approximations of the MSW resonance curve as well as the difference in χ^2 from the exponential (quadratic, cubic) best fit. The exponential and quadratic fits are consistent with a flat suppression as well as the MSW resonance "upturn." In either case an "upturn" fits slightly better (by about 1.0σ), but the coefficients describing the MSW resonance are actually slightly disfavored by 1.5σ (exponential) and 1.6σ (quadratic), for the best-fit Δm^2_{21} from KamLAND data, and by 0.8σ (exponential) and 0.7σ (quadratic) for the best-fit Δm^2_{21} from solar neutrino data. The cubic fit disfavors the flat suppression by 2.3σ; as seen in Fig. 27 the fit prefers an inflection point in the spectrum occurring near 8 MeV, a shape which cannot be accommodated by the other two parametrizations. From Table IX the SK-II and SK-IV minimum χ^2s of the cubic fit are similar to the quadratic and exponential fit, however the SK-I (SK-III) data favor the cubic fit by about 1.7σ (1.2σ). The reason for that preference is mostly due to data above $\sim$13 MeV (see Fig. 25). We checked these data but found no reason to exclude them. However, conservatively, we disregard the cubic best fit in our conclusions. Therefore, we find no significant spectral "upturn" (or downturn) at low energy, but our data is consistent with the "upturn" predicted by the MSW resonance curve (disfavoring the one based on solar + KamLAND best-fit parameters by about 1.5σ). Figure 25 shows the predictions for the best MSW fits, the best exponential/quadratic and the best cubic fit. Figure 26 statistically combines the different SK phases ignoring differences in energy resolutions and systematic uncertainties. It is

TABLE IX. Spectrum fit χ^2 comparison.

| Fit	MSW (sol + KamLAND)			MSW (solar)			Exponential			Quadratic			Cubic		
Param.	$\sin^2\theta_{12}, \sin^2\theta_{13}, \Delta m^2_{21}$ 0.304, 0.02, 7.50×10^{-5} eV^2			$\sin^2\theta_{12}, \sin^2\theta_{13}, \Delta m^2_{21}$ 0.304, 0.02, 4.84×10^{-5} eV^2			$e_0\ e_1, e_2$ 0.334, −0.001, −0.12			c_0, c_1, c_2 0.33, 0, 0.001			c_0, c_1, c_2, c_3 0.312, −0.031, 0.0095, 0.0044		
	χ^2	$\Phi_{^8B}/$ cm^2 sec	$\Phi_{hep}/$ cm^2 sec	χ^2	$\Phi_{^8B}/$ cm^2 sec	$\Phi_{hep}/$ cm^2 sec	χ^2	$\Phi_{^8B}/$ cm^2 sec	$\Phi_{hep}/$ cm^2 sec	χ^2	$\Phi_{^8B}/$ cm^2 sec	$\Phi_{hep}/$ cm^2 sec	χ^2	$\Phi_{^8B}/$ cm^2 sec	$\Phi_{hep}/$ cm^2 sec
SK-I	19.71	5.26×10^6	39.4×10^3	19.12	5.47×10^6	41.0×10^3	18.82	5.22×10^6	41.4×10^3	18.94	5.24×10^6	36.8×10^3	16.14	5.25×10^6	5.1×10^3
SK-II	5.39	5.33×10^6	55.1×10^3	5.35	5.53×10^6	56.8×10^3	5.31	5.27×10^6	56.9×10^3	5.38	5.30×10^6	51.5×10^3	5.15	5.34×10^6	11.9×10^3
SK-III	29.06	5.34×10^6	15.7×10^3	28.41	5.55×10^6	14.7×10^3	28.07	5.29×10^6	13.8×10^3	28.02	5.31×10^6	10.9×10^3	26.59	5.30×10^6	-3.6×10^3
SK-IV	14.43	5.22×10^6	12.2×10^3	14.00	5.44×10^6	11.4×10^3	14.29	5.20×10^6	10.8×10^3	14.15	5.22×10^6	8.2×10^3	14.07	5.22×10^6	-4.2×10^3
Combined	71.04	5.28×10^6	14.1×10^3	69.03	5.49×10^6	13.4×10^3	68.38	5.25×10^6	13.1×10^3	68.33	5.26×10^6	11.9×10^3	63.63	5.25×10^6	-0.7×10^3
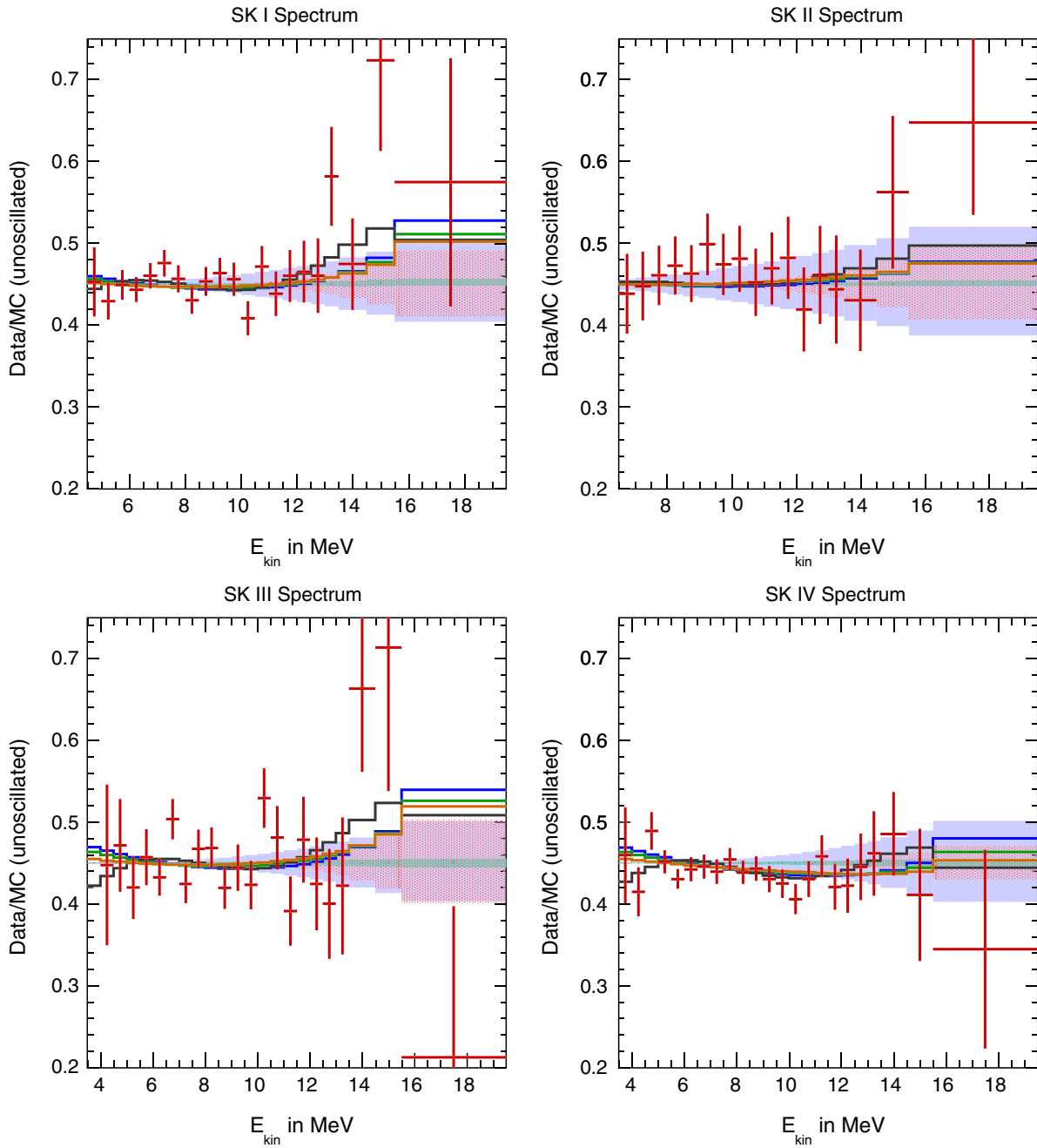
FIG. 25.   SK-I, II, III and IV recoil electron spectra divided by the nonoscillated expectation. The green (blue) line represents the best fit to SK data using the oscillation parameters from the fit to all solar (solar + KamLAND) data. The orange (black) line is the best fit to SK data of a general exponential or quadratic (cubic) P_{ee} survival probability. Error bars on the data points give the statistical plus systematic energy-uncorrelated uncertainties while the shaded purple, red, and green histograms give the energy-correlated systematic uncertainties arising from energy scale, energy resolution, and neutrino energy spectrum shift.

included only as an illustration and should not be fit to predictions.

Section B of the appendix discusses the measured coefficients, their uncertainties, and their correlations of all three parametrizations of P_{ee}. It also compares the quadratic coefficients obtained from SK data with those from SNO data, and the coefficients of the SK-SNO combined fit. Figure 27 compares the allowed survival probability P_{ee} based on the exponential fit with that based on the cubic and quadratic fits. Between about 5.5 and 12.5 MeV, the different parametrizations agree while outside this energy region parametrization-dependent extrapolation effects become significant. While the strength of the SK data constraints on P_{ee} is comparable

TABLE X. Spectrum fit χ^2 comparison for the "flat suppression" of 0.4268 of the expected rate assuming no neutrino oscillation.

Fit	With D/N correction			Without D/N correction		
	χ^2	$\Phi_{^8B}/\text{cm}^2$ sec	Φ_{hep}/cm^2 sec	χ^2	$\Phi_{^8B}/\text{cm}^2$ sec	Φ_{hep}/cm^2 sec
SK-I	18.92	5.38×10^6	41.4×10^3	18.81	5.47×10^6	42.6×10^3
SK-II	5.30	5.43×10^6	56.3×10^3	5.27	5.52×10^6	58.4×10^3
SK-III	27.94	5.45×10^6	12.0×10^3	27.98	5.55×10^6	13.1×10^3
SK-IV	15.50	5.37×10^6	9.4×10^3	14.99	5.46×10^6	10.2×10^3
Combined	69.30	5.41×10^6	12.3×10^3	68.75	5.50×10^6	12.7×10^3

to that of SNO data, its low energy constraints are tighter and its high energy constraints weaker. The reason for this is the absence of a nuclear threshold in elastic electron-neutrino scattering, and the direct correlation of neutrino energy and electron energy in neutrino-deuteron charged current interactions. SK data prefers a slight "upturn", SNO data prefer a "downturn." The combined fit favors an upturn more strongly than SK data by themselves since SK data prefer a higher average P_{ee} than SNO data, and the tighter SK constraints force the combined fit to this higher average probability at low energy, while the tighter SNO constrains force the combined fit to the lower SNO value at high energy. Figures 28 and 29 (combined fit) display the 1σ allowed bands of $P_{ee}(E_\nu)$. Figure 30 superimposes the same combined band (on a logarithmic scale) on the SSM [21] solar neutrino spectrum. Also shown are the pp and CNO neutrino flux constraints from all solar data [22] and the ^{7}Be, the pep and the ^{8}B flux measurement of the Borexino experiment [23]. The SK and SNO combined allowed band (and the other solar
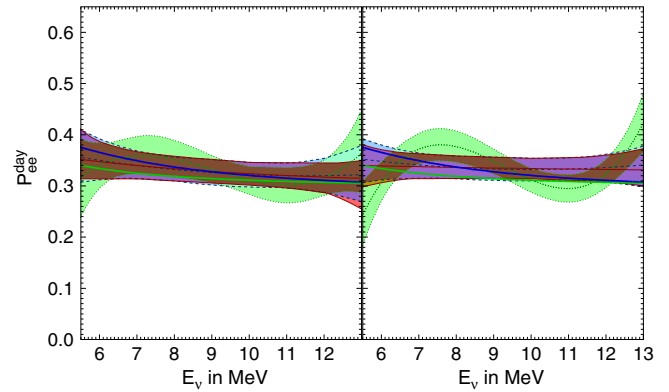

FIG. 27. Allowed survival probability 1σ band from SK-IV data (left) and all SK data (right). The red (blue) area is based on an exponential (quadratic) fit and the green band is based on a cubic fit. The ^{8}B flux is constrained to the measurement from SNO. The absolute value of the ^{8}B flux does not affect the shape constraint much, just the average value. Also shown are predictions based on the oscillation parameters of a fit to all solar data (green) and a fit to all solar + KamLAND data (blue).
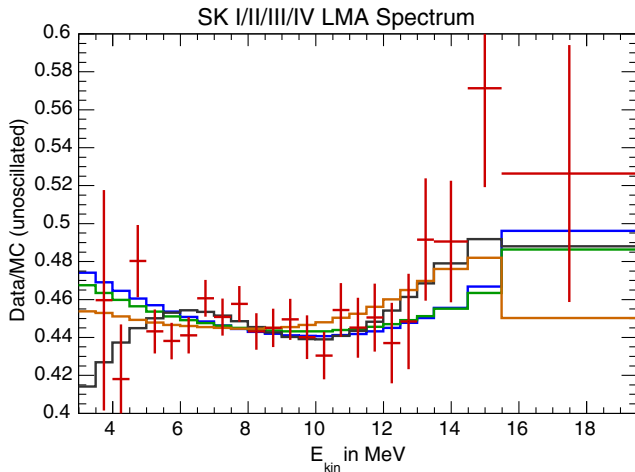
FIG. 26. SK-I + II + III + IV recoil electron spectrum compared to the no-oscillation expectation. The green (blue) shape is the MSW expectation using the SK (solar + KamLAND) best-fit oscillation parameters. The orange (black) line is the best fit to SK data with a general exponential/quadratic (cubic) P_{ee} survival probability.

FIG. 28. Allowed survival probability 1σ band from SK (solid green) and SNO (dotted blue) data. Also shown are predictions based on the oscillation parameters of a fit to all solar data (green) and a fit to all solar + KamLAND data (blue).

FIG. 29.　Allowed survival probability 1σ band from the combined data of SK and SNO (red). Also shown are predictions based on the oscillation parameters of a fit to all sola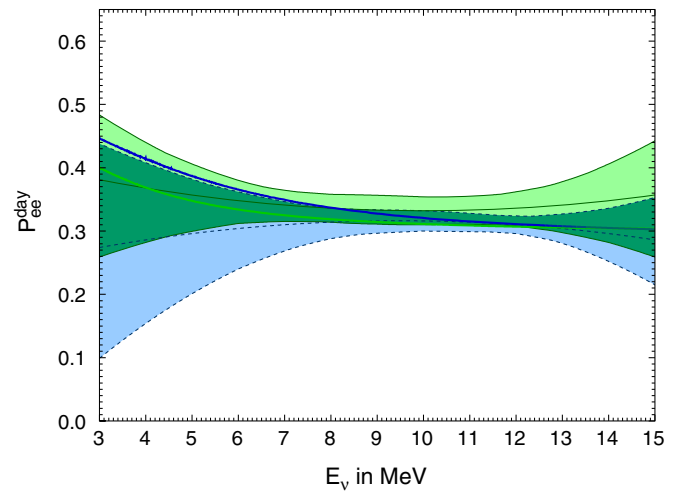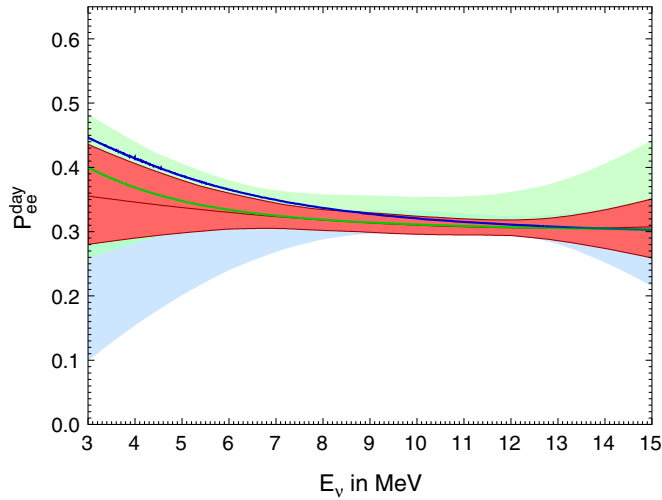r data (green) and a fit to all solar + KamLAND data (blue). The pastel colored bands are the separate SK (green) and SNO (blue) fits.
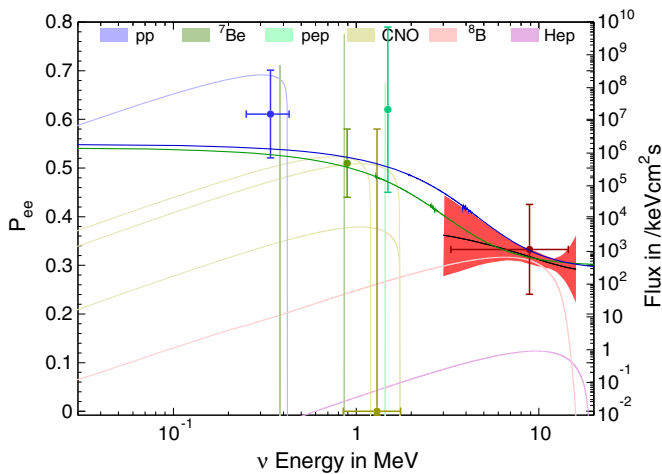

FIG. 30.　Predicted solar neutrino spectra [21]. Overlaid are expected MSW survival probabilities, green is that expected assuming oscillation parameters from the solar best fit and blue from the solar + KamLAND best fit. The 1σ band of P_{ee} from the combined data of SK and SNO is shown in red. Also shown are P_{ee} measurements of the ^{7}Be (green point), the pep (light green point) and the ^{8}B flux (red point) by Borexino [23], as well as pp (blue point) and CNO values (gold point) extracted from other experiments [22].

data) are in good agreement with the MSW curves (based on different parameters: blue = solar + KamLAND best fit, green = solar best fit).

V. DAY/NIGHT ASYMMETRY

The matter density of the Earth affects solar neutrino oscillations while the Sun is below the horizon. This

so called "day/night effect" will lead to an enhancement of the ν_e flavor content during the nighttime for most oscillation parameters. The most straightforward test of this effect uses the solar zenith angle θ_z (defined in Fig. 17) at the time of each event to separately measure the solar neutrino flux during the day Φ_D (defined as $\cos\theta_z \leq 0$) and the night Φ_N (defined as $\cos\theta_z > 0$). The day/night asymmetry $A_{DN} = (\Phi_D - \Phi_N)/\frac{1}{2}(\Phi_D + \Phi_N)$ defines a convenient measure of the size of the effect; it is sensitive to Δm^2_{21}.

A more sophisticated method to test the day/night effect is given in [1,24]. For a given set of oscillation parameters, the interaction rate as a function of the solar zenith angle is predicted. Only the shape of the calculated solar zenith angle variation is used; the amplitude is scaled by an arbitrary parameter. The extended maximum likelihood fit to extract the solar neutrino signal (see Sec. III C) is expanded to allow time-varying signals. The likelihood is then evaluated as a function of the average signal rates, the background rates and a scaling parameter, termed the "day/night amplitude". The equivalent day/night asymmetry is calculated by multiplying the fit scaling parameter with the expected day/night asymmetry. In this manner the day/night asymmetry is measured more precisely statistically and is less vulnerable to some key systematic effects.

Because the amplitude fit depends on the assumed shape of the day/night variation (given for each energy bin in [24] and [1]), it necessarily depends on the oscillation parameters, although with very little dependence expected on the mixing angles (in or near the large mixing angle solution and for θ_{13} values consistent with reactor neutrino measurements [25]). The fit is run for parameters covering the MSW region of oscillation parameters (10^{-9} eV$^2 \leq \Delta m^2_{21} \leq 10^{-3}$ eV^2 and $10^{-4} \leq \sin^2\theta_{12} < 1$), and values of $\sin^2\theta_{13}$ between 0.015 and 0.035.

A. Systematic uncertainty on the solar neutrino amplitude fit day/night flux asymmetry

1. Energy scale

True day (night) solar neutrino events will mostly be coming from the downward (upward) direction, and so the directional dependence of the SK light yield or energy scale will affect the observed interaction rate as a function of solar zenith angle and energy. To quantify the directional dependence of the energy scale, the energy of the DT-produced ^{16}N calibration data and its simulation are compared as a function of the reconstructed detector zenith angle (Fig. 9). The fit from Fig. 9 is used to shift the energy of the ^{8}B MC events, while taking energy-bin correlations into account, and the unbinned amplitude fit was rerun. The resulting 0.05% change in the equivalent day/night asymmetry is taken as

the systematic uncertainty coming from the directional dependence of the energy scale. The large reduction compared to SK-I (0.8%) comes from the use of a depth-dependent water transparency parameter, introduced at the beginning of SK-III. The further reduction from SK-III (0.2%) to SK-IV comes from an increase in DT calibration statistics and the improved timing agreement between data and MC, a result of the electronics upgrade.

2. Energy resolution

Throughout the different phases of SK, the energy resolution function relating the true and reconstructed recoil electron energies was found by two slightly different methods. During the SK-I and SK-IV phases, ^{8}B simulated events were used to set up a "transfer matrix" relating reconstructed to true recoil electron energy (and reconstructed recoil electron energy to neutrino energy.) This method, by construction, considers the effect of all analysis cuts on energy resolution. For the SK-II and III phases, dedicated monoenergetic simulated events were produced to parametrize the energy resolution with a Gaussian function, modeling only some analysis cuts. The two methods produce slightly different results; in particular, the predicted day/night asymmetries differ by 0.05%. To estimate the systematic uncertainty on the day/night asymmetry coming from the energy resolution function, the amplitude fit was performed using both methods, with the resulting 0.05% difference taken as the systematic uncertainty.

3. Background shape

Although there is only one background component fit in the day/night asymmetry fit (any time dependence of the background should be much slower than the day/night variation), different $\cos\theta_{sun}$ background shapes must be used for different solar zenith angle bins. We use one for the day and six for the night (in accordance with Table XII). The systematically different shapes come from the detector's directional bias when reconstructing background events (directions alongside and perpendicular to the detector symmetry axis are preferred). The background is first fit as functions of the detector zenith and azimuthal angles. These fits also yield a covariance matrix **V** for the fit parameters. The parameters of each of the zenith and azimuthal fits are varied by the one sigma statistical deviation, one at a time, giving a new background shape for each solar zenith angle bin. Because the background distributions are calculated as projections of the detector zenith and azimuthal angles on the solar direction, the shape deviations as a function of solar zenith angle are fully correlated and must be varied simultaneously. The day/night amplitude fit is then rerun for each set of new background shapes. The difference in the central value is taken as the error of the day/night asymmetry due to that

particular zenith or azimuthal fit parameter. These errors are then propagated to a total systematic uncertainty using the covariance matrix **V** of the fit to the detector zenith and azimuth angles. The total uncertainty on the day/night asymmetry coming from the background shapes is 0.6%, and is the largest contribution to the total.

4. Event selection

Most of the analysis cuts affect the day and night solar neutrino interaction rates equally, so their effect on the systematic uncertainty on the day/night asymmetry can be neglected. However, the vertex shift and angular resolution difference between data and simulated events can cause a bias in the external event cut efficiency when used in conjunction with the tight fiducial volume cut. To estimate the size of the effect, we artificially shift the reconstructed vertex and direction and estimate the fraction of events which are rejected by the cuts during daytime and during nighttime. The associated estimated systematic uncertainty is ±0.1%.

5. Earth model

Different models of Earth's density profile can change the signal rate zenith profiles, thus leading to changes in the measured day/night asymmetry value. For this reason it is essential to model the Earth as precisely as possible, most frequently done using the Preliminary Reference Earth Model (PREM) [26] and an Earth which is assumed to be spherical. A spherical description of Earth using the equatorial radius leads to a ∼0.2% change in the day/night effect from a spherical description using an average radius. To better represent the Earth we have modeled an ellipsoidal Earth, using the equatorial and polar radii as the semimajor and semiminor axes of an ellipse. The ellipse is then rotated around its minor axis to produce an ellipsoid and the spherical PREM model density boundaries are mapped accordingly.

Due to SK's location on Earth and using the above procedure of modeling an ellipsoidal Earth, the event rate is no longer rotationally symmetric about the detector azimuthal angle and the day/night zenith amplitude fit must take into account the change in the expected signal rate as the azimuthal angle is varied. This was done by varying the azimuthal angle and the zenith angle when tracing neutrinos through the Earth, and then using the detector livetime to average over the azimuthal angle. The resulting expected solar zenith angle dependent signal rates were then used in the day/night amplitude fit and the results compared to the results when assuming a spherical Earth with an average radius. The 0.01% change in the day/night asymmetry is taken as the systematic uncertainty coming from the Earth shape.

As a final step in estimating the systematic uncertainty coming from the model of the Earth, the PREM model was replaced with the more recent PREM500 model [27], which

gives an updated and more detailed description of the density profile of Earth. This resulted in a 0.01% shift in the measured day/night asymmetry. When added in quadrature to the uncertainty coming from the Earth shape, 0.014% gives the total estimated uncertainty coming from the Earth model.

6. Summary of the systematic uncertainty

The total estimated systematic uncertainty on the measured day/night asymmetry is calculated by adding the components in quadrature, the result of which can be seen in Table XI. The large reduction in systematics from SK-I [1] to SK-IV comes from the introduction of a z-dependent absorption into the simulation and a better method of estimating the systematic uncertainty using DT data. The directional dependence of the energy scale is now better understood, bringing the total systematic uncertainty to $\pm 0.6\%$.

B. SK day/night asymmetry results

The SK-IV livetime during the day (night) is 797 days (866 days). The solar neutrino flux between 4.49 and 19.5 MeV assuming no oscillations is measured as $\Phi_D = (2.250^{+0.030}_{-0.029}(\text{stat}) \pm 0.038(\text{sys})) \times 10^6/(\text{cm}^2 \text{ sec})$ during the day and $\Phi_N = (2.364 \pm 0.029(\text{stat}) \pm 0.040(\text{sys})) \times 10^6/(\text{cm}^2 \text{ sec})$ during the night. Figure 31 shows the solar zenith angle variation of the ratio of the measured rate to the unoscillated simulated rate (assuming $5.25 \times 10^6/(\text{cm}^2 \text{ sec})$ for the ^{8}B flux) in the seven energy regions shown in Table XII. Overlaid is the expected zenith variation for best-fit oscillation parameters coming from a fit to all solar neutrino data (solar + KamLAND data) in red (blue). Table XII lists the data used in Fig. 31, the errors are statistical uncertainties only. Figure 32 shows the data over simulated rate ratio between 4.49 and 19.5 MeV (assuming no oscillations) as a function of $\cos\theta_z$, divided into five day and six night bins (corresponding to the mantle 1–5 and core definitions of Table XII). By comparing the separately measured day and night fluxes, the measured day/night asymmetry for SK-IV is found to be $A_{\text{DN}} = (-4.9 \pm 1.8(\text{stat}) \pm 1.4(\text{sys}))\%$.

TABLE XI. SK-IV amplitude fit day/night asymmetry systematic uncertainties. The total is found by adding the contributions in quadrature.

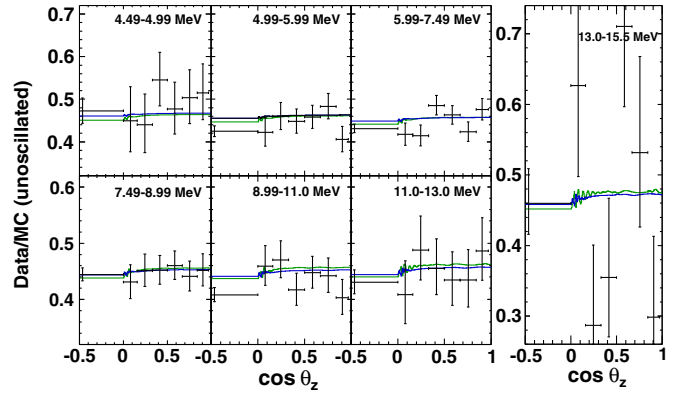|	
Energy scale	0.05%
Energy resolution	0.05%
Background shape	0.6%
Event selection	0.1%
Earth model	0.01%
Total	0.6%

FIG. 31. SK-IV data/MC (unoscillated) rate dependence on the solar zenith angle, for various energy regions (zenith angle and energy bins defined in Table XII, panels are ordered by energy with the upper, left panel being the lowest). The unoscillated rate assumes a ^{8}B (hep) flux of $5.25 \times 10^6/(\text{cm}^2 \text{ sec})$ $(8 \times 10^3/(\text{cm}^2 \text{ sec}))$. Overlaid green (blue) lines are predictions when using the solar neutrino data (solar neutrino data + KamLAND) best-fit oscillation parameters and the assumed neutrino fluxes fit to best describe the data. The error bars shown are statistical uncertainties only.

The SK-IV day/night asymmetry resulting from the day/night amplitude fit method, for an energy range of 4.49–19.5 MeV and oscillations parameters preferred by SK ($\Delta m^2_{21} = 4.84 \times 10^{-5} \text{ eV}^2$, $\sin^2\theta_{12} = 0.311$ and $\sin^2\theta_{13} = 0.020$), is found to be

$$A_{\text{DN}}^{\text{fit,SK-IV}} = (-3.6 \pm 1.6(\text{stat}) \pm 0.6(\text{syst}))\%.$$

The expected day/night asymmetry for the above set of oscillation parameters is -3.3%. For the case of a global fit to solar neutrino data and KamLAND [3], the mass squared splitting changes to $\Delta m^2_{21} = 7.50 \times 10^{-5} \text{ eV}^2$, and the expected day/night asymmetry goes to -1.7%. However, the day/night amplitude fit measured SK-IV day/night asymmetry is only slightly reduced to

$$A_{\text{DN}}^{\text{fit,SK-IV}} = (-3.3 \pm 1.5(\text{stat}) \pm 0.6(\text{syst}))\%.$$

Within the Δm^2_{21} range of the large mixing angle (LMA) region, all measured values of the day/night asymmetry coming from the day/night amplitude fit are within $\pm 0.3\%$ of -3.3%. If the above measurement is combined with the previous three phases of SK, the SK combined measured day/night asymmetry is

$$A_{\text{DN}}^{\text{fit,SK}} = (-3.3 \pm 1.0(\text{stat}) \pm 0.5(\text{syst}))\%.$$

Previously, we published $A_{\text{DN}}^{\text{fit,SK}} = (-3.2 \pm 1.1(\text{stat}) \pm 0.5(\text{syst}))\%$ in [28] which was the first significant

TABLE XII. The observed zenith angle dependence of event rates (events/year/kton) in each energy region, at 1 AU. The errors are statistical uncertainties only. The reduction efficiencies are corrected and the expected event rates are for a flux of $5.25 \times 10^6/(\text{cm}^2 \text{ sec})$.

Energy (MeV)	DAY $\cos\theta_z = -1 \sim 0$	MANTLE1 $0 \sim 0.16$	MANTLE2 $0.16 \sim 0.33$	MANTLE3 $0.33 \sim 0.50$	MANTLE4 $0.50 \sim 0.67$	MANTLE5 $0.67 \sim 0.84$	CORE $0.84 \sim 1$	Unoscillated rate ^{8}B	hep
				Observed rate					
4.49–4.99	$79.4^{+5.1}_{-5.0}$	$75.5^{+13.4}_{-12.2}$	$74.5^{+12.1}_{-11.1}$	$91.6^{+10.9}_{-10.2}$	$80.3^{+10.6}_{-10.3}$	$85.1^{+11.1}_{-10.3}$	$86.9^{+11.4}_{-10.6}$	167.8	0.323
4.99–5.99	$124.2^{+3.8}_{-3.7}$	$116.8^{+9.5}_{-9.0}$	$127.0^{+8.9}_{-8.5}$	$123.9^{+8.0}_{-7.6}$	$126.7^{+7.7}_{-7.4}$	$133.9^{+8.4}_{-8.1}$	$112.3^{+8.5}_{-8.1}$	283.6	0.611
5.99–7.49	$139.5^{+3.3}_{-3.2}$	$134.2^{+8.6}_{-8.2}$	$133.3^{+8.1}_{-7.7}$	$155.7^{+7.5}_{-7.2}$	$148.5^{+7.1}_{-6.9}$	$136.1^{+7.5}_{-7.2}$	$153.0^{+8.3}_{-7.9}$	321.4	0.799
7.49–8.99	$93.5^{+2.7}_{-2.7}$	$89.3^{+7.1}_{-6.6}$	$90.5^{+6.7}_{-6.3}$	$88.6^{+5.9}_{-5.6}$	$94.0^{+5.8}_{-5.6}$	$88.1^{+6.2}_{-5.9}$	$102.2^{+7.2}_{-6.8}$	196.6	0.647
8.99–11.0	$52.0^{+1.8}_{-1.8}$	$55.7^{+5.1}_{-4.7}$	$57.8^{+4.7}_{-4.4}$	$47.7^{+4.0}_{-3.7}$	$54.4^{+4.0}_{-3.7}$	$56.4^{+4.4}_{-4.1}$	$65.5^{+5.1}_{-4.8}$	122.2	0.619
11.0–13.0	$15.5^{+0.9}_{-0.9}$	$17.4^{+2.6}_{-2.2}$	$17.3^{+2.5}_{-2.1}$	$15.3^{+2.0}_{-1.8}$	$14.9^{+2.0}_{-1.7}$	$15.2^{+2.2}_{-1.9}$	$17.7^{+2.5}_{-2.2}$	36.0	0.365
13.0–15.5	$3.83^{+0.46}_{-0.40}$	$5.69^{+1.54}_{-1.18}$	$2.53^{+1.07}_{-0.73}$	$2.49^{+0.91}_{-0.65}$	$4.19^{+1.03}_{-0.80}$	$3.84^{+1.15}_{-0.86}$	$4.48^{+1.33}_{-1.01}$	7.45	0.204

indication that matter effects influence neutrino oscillations. The slightly larger significance (2.9σ) here is due to a somewhat larger data set.

VI. OSCILLATION ANALYSIS

SK measures elastic scattering of solar neutrinos with electrons, the rate of which depends on the flavor content of the solar neutrino flux, so it is sensitive to neutrino flavor oscillations. To constrain the parameters governing these oscillations, we analyze the integrated scattering rate, the recoil electron spectrum (which statistically implies the

FIG. 32. SK-IV solar zenith angle dependence of the solar neutrino data/MC (unoscillated) interaction rate ratio (4.49–19.5 MeV). The day data are subdivided into five bins, while the night data are divided into six bins. Solar neutrinos in the last night bin pass through the Earth's outer core. Overlaid green (blue) lines are predictions when using the solar neutrino data (solar neutrino data + KamLAND) best-fit oscillation parameters and the assumed neutrino fluxes fit to best describe the data. The error bars shown are statistical uncertainties only.

energy-dependence of the electron-flavor survival probability), and the time of the interactions which defines the neutrino path through the earth during night time, and therefore controls the earth matter effects on solar neutrino oscillations. An expansion of the likelihood used in the extended maximum likelihood fit to extract the solar neutrino signal (see Sec. III C) could make full use of *all* information (timing, spectral information and rate), but is CPU time intensive. Instead, we separate the log(likelihood) into a time-variation (day/night variation) portion $\log\mathcal{L}_{\text{DN}}$ and a spectral portion: $\log\mathcal{L} = \log\mathcal{L}_{\text{DN}} + \log\mathcal{L}_{\text{spec}}$ where $\mathcal{L}_{\text{spec}}$, the likelihood for assuming no time variation, is replaced by $-\frac{1}{2}\chi^2_{\text{spec}}$. This χ^2_{spec} fits the calculated elastic scattering rate in energy bin e of a particular SK phase p to the measurement $d^p_e \pm \sigma^p_e$. The calculated event rate r^p_e is the sum of the expected elastic scattering rate b^p_e from ^{8}B neutrinos scaled by the parameter β and hep from hep neutrinos scaled by the parameter η: $r^p_e = \beta b^p_e + \eta h^p_e$. The calculation includes neutrino flavor oscillations of three flavors; they depend on the mixing angles θ_{12}, θ_{13} and the mass squared difference Δm^2_{21}. r^p_e is then multiplied by the spectral distortion factor $f^p_e(\tau, \epsilon_p, \rho_p)$ which describes the effect of a systematic shift of the ^{8}B neutrino spectrum scaled by the constrained nuisance parameter τ, a deviation in the SK energy scale in phase p described by the constrained nuisance parameter ϵ_p, and a systematic change in the SK energy resolution based on a third constrained nuisance parameter ρ_p. If N_p is the number of energy bins of phase p, we minimize

$$\chi^2_P(\beta, \eta) = \sum_{e=1}^{N_p} \left(\frac{d^p_e - f^p_e r^p_e (\sin^2\theta_{12}, \sin^2\theta_{13}, \Delta m^2_{21})}{\sigma^p_e} \right)^2$$

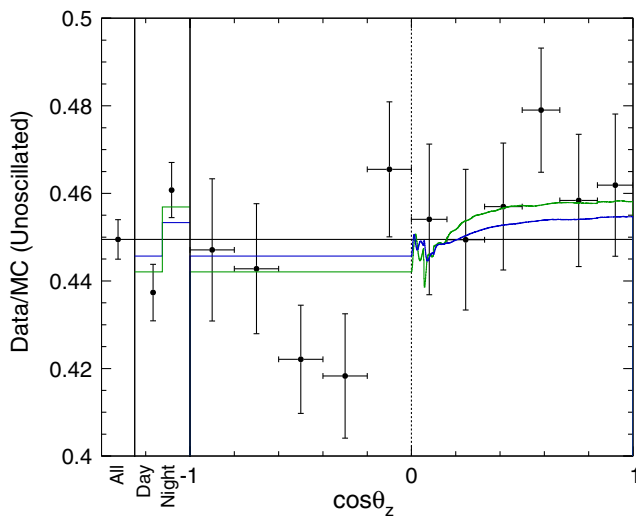over all systematic nuisance parameters and the flux scaling parameters:

$$\chi^2_{\text{spec},1} = \underset{\tau,\epsilon_p,\rho_p,\beta,\eta}{\text{Min}} \left(\chi^2_{p,\text{dat}} + \tau^2 + \epsilon_p^2 + \rho_p^2 + \Phi\right), \quad (6.1)$$

where $\Phi = \left(\frac{\beta-\beta_0}{\sigma_\beta}\right)^2 + \left(\frac{\eta-\eta_0}{\sigma_\eta}\right)^2$ constrains the flux parameters to prior uncertainties: β is constrained to result in a ^{8}B flux of $(5.25 \pm 0.20) \times 10^6/(\text{cm}^2\,\text{sec})$ (motivated by the SNO NC measurement of the total ^{8}B neutrino flux [19]), η is only slightly constrained to correspond to a hep flux of $(8 \pm 16) \times 10^3/(\text{cm}^2\,\text{sec})$. The nuisance parameters τ, ϵ_p, and ρ_p are constrained to 0 ± 1 (i.e. they are defined as standard Gaussian variables) by the "penalty terms" $\left(\frac{\tau-0}{1}\right)^2$, $\left(\frac{\epsilon_p-0}{1}\right)^2$, and $\left(\frac{\rho_p-0}{1}\right)^2$. We rewrite Eq. (6.1) as a quadratic form with the 2×2 curvature matrix $\mathbf{C}_p$ and the best-fit flux parameters β^p_{min} and η^p_{min} as

$$\chi^2_{\text{spec},\alpha_p} = \chi^2_{p,\text{min}} + \alpha_p(\beta - \beta^p_{\text{min}}, \eta - \eta^p_{\text{min}})$$
$$\cdot \mathbf{C}_p \cdot \begin{pmatrix} \beta - \beta^p_{\text{min}} \\ \eta - \eta^p_{\text{min}} \end{pmatrix}, \quad (6.2)$$

for $\alpha_p = 1$. The parameter $\alpha_p \neq 1$ is introduced to scale the *a posteriori* constraints on the flux parameters by $1/\sqrt{\alpha_p}$ without affecting the χ^2 minimum in order to take into account additional systematic uncertainties of the total rate. These uncertainties are not covered by σ_e^p or f_e^p. Table V (subtotal) lists these additional uncertainties integrated over all energies. To incorporate them we choose $\alpha_p = \frac{\sigma^2_{p,\text{stat}}}{\sigma^2_{p,\text{stat}}+\sigma^2_{p,\text{syst}}}$. To best compare this three-flavor analysis to two-flavor analyses performed for previous phases, we also perform an analysis with an *a priori* constraint on θ_{13}

coming from reactor neutrino experiments [25]. Unlike the two-flavor analyses, θ_{13} is not fixed to zero, but constrained to a nonzero value by $\left(\frac{\sin^2\theta_{13}-0.0219}{0.0014}\right)^2$. The time-variation likelihood $\log\mathcal{L}_{\text{DN}} = \log\mathcal{L}_{\text{with}} - \log\mathcal{L}_{\text{without}}$ is simply the difference between the likelihoods with and without the predicted day/night variation *assuming* the best-fit flux and nuisance parameters from the spectrum χ^2 minimization. As the uncertainties in each spectral bin are closely approximated by Gaussian uncertainties, the total χ^2 is then given by $\chi^2_{\text{spec}} - 2\log\mathcal{L}_{\text{DN}}$. Figure 33 shows allowed regions of oscillation parameters from SK-IV data with the external constraint from reactor neutrino data on θ_{13} at the 1, 2, 3, 4, and 5σ confidence level. SK-IV determines $\sin^2\theta_{12}$ to be $0.327^{+0.026}_{-0.031}$, as well as Δm^2_{21} to be $(3.2^{+2.8}_{-0.2}) \times 10^{-5}$ eV^2. A secondary region appears at about the 3σ level at $\Delta m^2_{21} \approx 8 \times 10^{-8}$ eV^2. Small mixing is only very marginally allowed at about the 5σ confidence level.

We combined the SK-IV constraints with those of previous SK phases, as well as other solar neutrino experiments [19,22]. For the combined SK fit, the spectrum and rate χ^2 is

$$\chi^2_{\text{spec}} = \underset{\nu,\epsilon_p,\rho_p,\beta,\eta}{\text{Min}} \left(\sum_{p=1}^{4}\chi^2_{p,\alpha_p} + \tau^2 + \sum_{p=1}^{4}(\epsilon_p^2 + \rho_p^2) + \Phi\right). \quad (6.3)$$

Each SK phase is represented by a separate day/night likelihood ratio, where the flux and nuisance parameters are taken from the combined fit. Figure 33 shows the SK combined allowed areas based on rate, spectrum, and
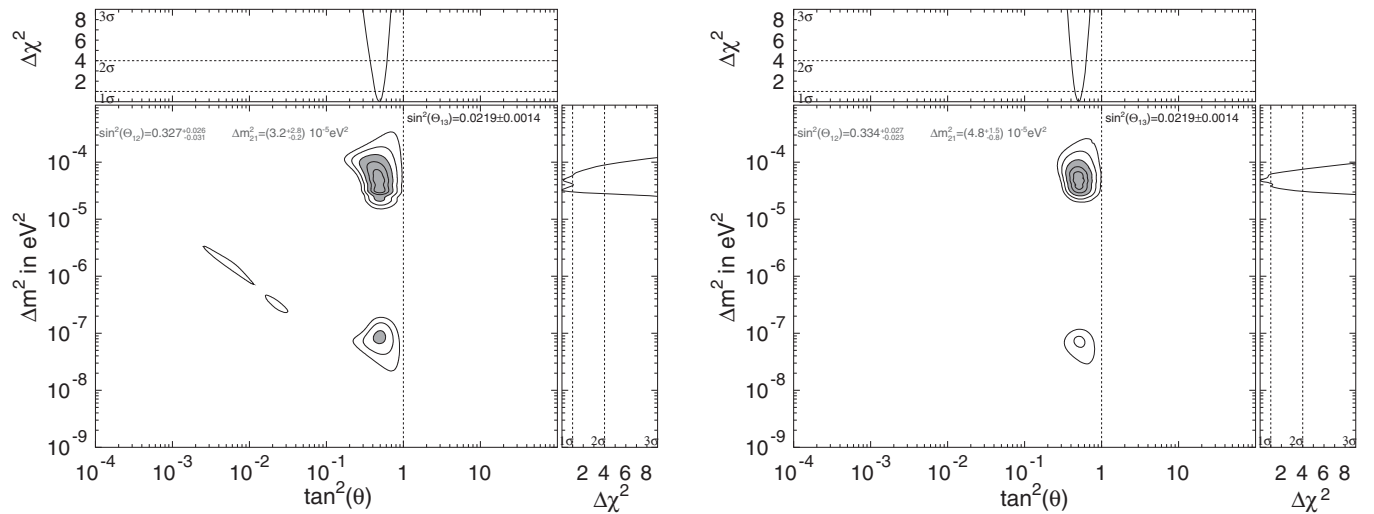
FIG. 33. Contours of Δm^2_{21} vs $\tan^2\theta_{12}$ from the SK-IV (left panel) and SK-I/II/III/IV (right panel) spectral + day/night data with a ^{8}B flux constraint of $5.25 \pm 0.20 \times 10^6/(\text{cm}^2\,\text{sec})$ at the 1, 2, 3, 4, and 5σ confidence levels. The filled regions give the 3σ confidence level results. θ_{13} is constrained by $\left(\frac{\sin^2\theta_{13}-0.0219}{0.0014}\right)^2$.
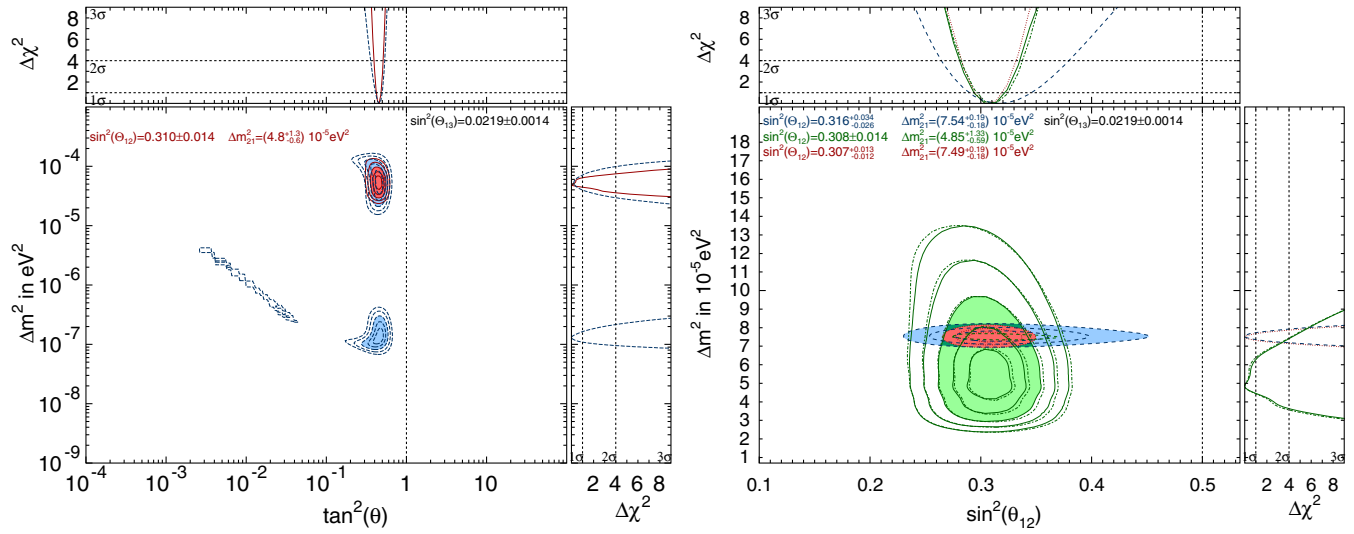
FIG. 34. Left: comparison of the oscillation parameter determination of the SK and SNO combined analysis (red) to the oscillation constraints of SNO by itself (blue). Right: allowed contours of Δm^2_{21} vs $\sin^2 \theta_{12}$ from solar neutrino data (green), KamLAND data (blue), and the combined result (red). For comparison, the almost identical result of the SK + SNO combined fit is shown by the dashed dotted lines. The filled regions give the 3σ confidence level results, the other contours shown are at the 1 and 2σ confidence level (for the solar analyses, 4 and 5σ confidence level contours are also displayed). θ_{13} is constrained by $\left(\frac{\sin^2 \theta_{13} - 0.0219}{0.0014}\right)^2$.

day/night variation. SK selects large mixing ($0.5 > \sin^2 \theta_{12} > 0.2$) over small mixing by more than five standard deviations and very strongly (3.6σ) favors the Δm^2_{21} of the LMA solution (below 2×10^{-4} eV^2 and above 2×10^{-5} eV^2) over any other oscillation parameters. SK determines $\sin^2 \theta_{12}$ to be $0.334^{+0.027}_{-0.023}$, as well as Δm^2_{21} to be $(4.8^{+1.5}_{-0.8}) \times 10^{-5}$ eV^2.

Figure 34 compares the SK + SNO combined constraints to those based on SNO data alone [19]. While SNO's measurement of the mixing angle is more precise ($\sin^2 \theta_{12} = 0.299^{+0.023}_{-0.020}$) than SK's, its Δm^2_{21} constraints are poorer [$(5.6^{+1.9}_{-1.4}) \times 10^{-5}$ eV^2]. Also, SNO very slightly favors the low mass (Low) solution (region near 10^{-7} eV^2) and allows small mixing at the 3.6σ level. The combined analysis of SK and SNO is particularly powerful: as SNO and SK both measure ^{8}B neutrinos in a very similar energy range but in a different way and with different systematic effects, the combined analysis profits from correlations and is better than a mere addition of χ^2's. The SK + SNO combined analysis measures $\sin^2 \theta_{12} = 0.310 \pm 0.014$ and $\Delta m^2_{21} = (4.8^{+1.3}_{-0.6}) \times 10^{-5}$ eV^2. Oscillation parameter values outside the LMA are very strongly excluded: the solar mixing angle lies within $0.12 \leq \sin^2 \theta_{12} \leq 0.45$ at about the 7.5σ C.L., $\Delta m^2_{21} < 1.33 \times 10^{-5}$ eV^2 (which includes the "small mixing angle" and "low mass" regions) is ruled out at the 5.5σ C.L., and $\Delta m^2_{21} > 1.9 \times 10^{-4}$ eV^2 is excluded at 7.5σ C.L. The *hep* flux constraint used by SNO is $(7.9 \pm 1.2) \times 10^3 /(\text{cm}^2 \text{ sec})$ from the solar standard model [21]. The SK and SNO combined analysis also uses this tighter constraint.

The combined allowed contours based on SK, SNO [19] and other solar neutrino experiments' [22] data, KamLAND's constraints and the combination of the two are shown in Figs. 34 and 35. SK and SNO dominate the combined fit to all solar neutrino data. This can be seen from the two almost identical sets of green contours in Fig. 34. The low energy measurement of the ^{7}Be day/night asymmetry [29] does not change the
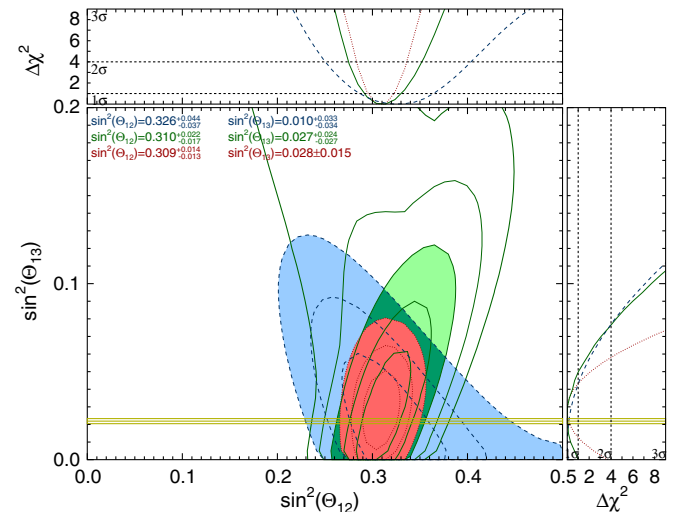

FIG. 35. Allowed contours of $\sin^2 \theta_{13}$ vs $\sin^2 \theta_{12}$ from solar neutrino data (green) at 1, 2, 3, 4, and 5σ and KamLAND measurements (blue) at the 1, 2, and 3σ confidence levels. Also shown is the combined result in red. The yellow band is the θ_{13} measurement from reactor neutrino data [25].

constraints in the LMA region, but independently excludes the Low solution. In the right panel of this figure, some tension between the solar neutrino and reactor antineutrino measurements of the solar Δm_{21}^2 is evident, stemming from the SK day/night measurement. Even though the expected day/night amplitude agrees within $\sim 1.1\sigma$ with the fitted amplitude for any Δm_{21}^2, in either the KamLAND or the SK range, the SK data slightly favor the shape of the day/night variation predicted by values of Δm_{21}^2 that are smaller than KamLAND's. Figure 35 shows the results of the θ_{13} unconstrained fit. Solar neutrinos by themselves weakly favor a nonzero θ_{13} by about one standard deviation because for low energy solar neutrinos the survival probability (e.g ^{7}Be) is about $(1 - \frac{1}{2}\sin^2(2\theta_{12}))\cos^4(\theta_{13})$ while the MSW effect causes a high energy (^{8}B) solar neutrino survival probability of $\sin^2(\theta_{12})\cos^4(\theta_{13})$. This results in a correlation of $\sin^2(\theta_{12})$ and $\sin^2(\theta_{13})$ for high energy neutrinos and an anticorrelation for low energy neutrinos. KamLAND reactor neutrino data has the same anticorrelation as the low energy solar neutrinos because in both cases matter effects play a minor role. Therefore the significance of nonzero θ_{13} increases in the solar + KamLAND data combined fit to $\sim 2\sigma$, favoring $\sin^2\theta_{13} = 0.028 \pm 0.015$.

VII. CONCLUSION

The fourth phase of SK measured the solar ^{8}B neutrino-electron elastic scattering-rate with the highest precision yet. SK-IV measured a solar neutrino flux of $(2.308 \pm 0.020(\text{stat})^{+0.039}_{-0.040}(\text{syst})) \times 10^6/(\text{cm}^2 \text{ sec})$ assuming no oscillations. When combined with the results from the previous three phases, the SK combined flux is $(2.345 \pm 0.014(\text{stat}) \pm 0.036(\text{syst})) \times 10^6/(\text{cm}^2 \text{ sec})$. A quadratic fit of the electron-flavor survival probability as a function of energy to all SK data, as well as a combined fit with SNO solar neutrino data, very slightly favor the presence of spectral distortions, but are still consistent with an energy-independent electron neutrino flavor content. The SK-IV solar neutrino elastic scattering day/night rate asymmetry is measured as $(-3.6 \pm 1.6(\text{stat}) \pm 0.6(\text{syst}))\%$. Combining this with other SK phases, the SK solar zenith angle variation data gives the first significant indication for matter-enhanced neutrino oscillation: the significance compared to no day/night asymmetry is 2.9σ. This leads SK to having the world's most precise measurement of $\Delta m_{21}^2 = (4.8^{+1.5}_{-0.8}) \times 10^{-5}$ eV^2, using neutrinos rather than antineutrinos. There is a slight tension of 1.5σ between this value and KamLAND's measurement using reactor antineutrinos. The tension increases to 1.6σ, if other solar neutrino data are included. The SK-IV solar neutrino data determine the solar mixing angle as $\sin^2\theta_{12} = 0.327^{+0.026}_{-0.031}$, all SK solar data measures this angle

to be $\sin^2\theta_{12} = 0.334^{+0.027}_{-0.023}$, the determined squared splitting is $\Delta m_{21}^2 = 4.8^{+1.5}_{-0.8} \times 10^{-5}$ eV^2. A θ_{13} constrained fit to all solar neutrino data and KamLAND yields $\sin^2\theta_{12} = 0.307^{+0.013}_{-0.012}$ and $\Delta m_{21}^2 = (7.49^{+0.19}_{-0.18}) \times 10^{-5}$ eV^2. When this constraint is removed, solar neutrino experiments and KamLAND measure $\sin^2\theta_{13} = 0.028 \pm 0.015$, a value in good agreement with reactor neutrino measurements.

APPENDIX A: REVISED SK-III RESULTS

Since the publication of the previous report [9], two mistakes were found. One is in how energy-dependent systematic errors are calculated and the other is related to the flux calculation in SK-III. The estimates of the energy-correlated uncertainties in the main text of that report are based on the Monte Carlo (MC) simulated ^{8}B solar neutrino events. It is found that this evaluation method was not accurate enough. The statistical error of the MC
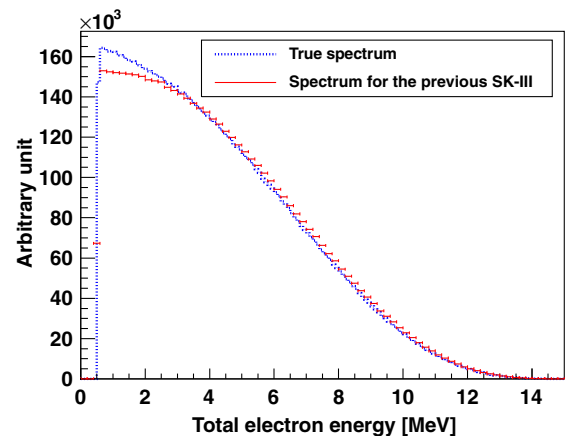

FIG. 36. Energy spectrum shapes of recoil electrons from ^{8}B solar neutrinos for SK-III. The blue dotted and red solid lines show the true theoretical calculation and incorrect spectrum used in the SK-III analysis in the previous report [9].

simulation distorted the shapes of the energy-correlated uncertainties systematically.

The energy dependence of the differential interaction cross section between neutrinos and electrons was accidentally eliminated only for the SK-III flux calculation in the main text. Figure 36 shows the energy distributions of recoil electrons from ^{8}B solar neutrinos. The blue dotted histogram shows the true energy spectrum shape from a theoretical calculation considering the detector resolutions. The red solid plot shows the energy spectrum shape used in the SK-III analysis in the previous report. The expected total flux was normalized correctly, but the expected ^{8}B energy spectrum shape was improperly distorted in the analysis.

These mistakes have been fixed in this paper. In this appendix, the revised SK-III solar neutrino results are described. The latest oscillation results, including both revised SK-III data and SK-IV data, are reported in the main text of this report.

1. Systematic uncertainties

The energy-correlated systematic uncertainties are obtained by counting the number of events in the solar neutrino MC simulation with artificially shifted energy scale, energy resolution and ^{8}B solar neutrino energy spectrum. In the SK-III analysis in the previous report, this estimation was done with the generated solar neutrino MC events. However, in the high energy region, not enough MC events were generated to accurately estimate the small systematic errors. In the current analysis, this estimation is performed with a theoretical calculation considering the detector resolutions, thus eliminating the statistical effects introduced by the small MC statistics.
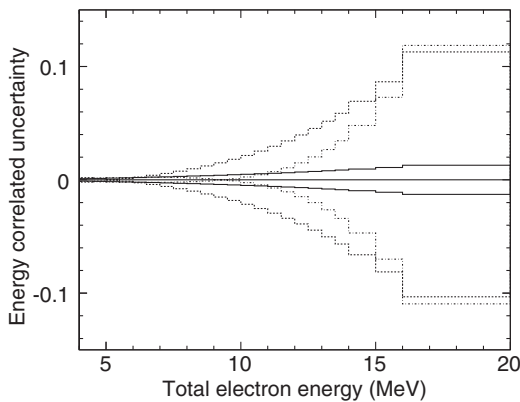
FIG. 37   Revised energy-correlated systematic uncertainties in SK-III. The solid, dotted, and dashed lines show the uncertainties of the ^{8}B spectrum, the energy scale, and the energy resolution, respectively. This is a revision of Fig. 25 in the previous paper [9].

TABLE XIII   Revised summary of the systematic uncertainty of the total flux in $E_{total} = 5.0–20.0$ MeV in SK-III. This is a revision of Table IV in the previous paper [9].

Source	Total Flux
Energy scale	±1.4%
Energy resolution	±0.2%
^{8}B spectrum	±0.4%
Trigger efficiency	±0.5%
Angular resolution	±0.67%
Vertex shift	±0.54%
Event quality cuts	
- Reconstruction Goodness	±0.4%
- Hit pattern	±0.25%
- Second vertex	±0.45%
Spallation cut	±0.2%
Gamma-ray cut	±0.25%
Cluster hit cut	±0.5%
Background shape	±0.1%
Signal extraction	±0.7%
Livetime	±0.1%
Cross section	±0.5%
Total	±2.2%

The revised results of the energy-correlated systematic uncertainties are shown in Fig. 37. In this update, the uncertainty from ^{8}B spectrum shape was improved.

The systematic uncertainties on total flux in SK-III are also revised. The revised uncertainties are summarized in Table XIII. The ^{8}B spectrum error was underestimated in the analysis in the main text of [9]. The revised systematic uncertainty on the total flux in $E_{total} = 5.0–20.0$ MeV in SK-III is estimated to be 2.2%.

2. ^{8}B solar neutrino flux results

The observed number of solar neutrino events is also updated. In this analysis, the extracted number of ^{8}B solar neutrinos with the ES reaction in $E_{total} = 5.0–20.0$ MeV for a live time of 548 days of SK-III data was $8148^{+133}_{-131}(\text{stat}) \pm 176(\text{sys})$. The corresponding ^{8}B flux is obtained to be:

$$2.404 \pm 0.039(\text{stat}) \pm 0.053(\text{sys}) \times 10^6 \text{ cm}^{-2}\text{sec}^{-1}.$$

Fixing the cross section problem, a 3.4% increase was observed.

The observed and expected fluxes are reestimated in each energy region. Table XIV shows the revised event rate in each energy region. Figure 38 shows the revised observed energy spectrum divided by the 5.79×10^6 cm^{-2}sec^{-1} flux value without oscillations.

TABLE XIV   Revised observed energy spectra expressed in units of event/kton/year in SK-III in each recoil electron total energy region. The errors in the observed rates are statistical only. The expected rates neglecting oscillations are for a flux value of 5.79×10^6 cm^{-2} sec^{-1}. θ_z is the angle between the z-axis of the detector and the vector from the Sun to the detector. This is a revision of Table VI in the previous paper [9].

Energy (MeV)	Observed rate			Expected rate	
	ALL $-1 \leq \cos\theta_z \leq 1$	DAY $-1 \leq \cos\theta_z \leq 0$	NIGHT $0 < \cos\theta_z \leq 1$	^{8}B	hep
5.0–5.5	$82.3^{+10.3}_{-9.9}$	$93.4^{+15.7}_{-14.9}$	$72.6^{+13.7}_{-13.0}$	189.7	0.334
5.5–6.0	$66.4^{+6.4}_{-6.1}$	$73.7^{+9.8}_{-9.3}$	$59.9^{+8.4}_{-7.9}$	172.2	0.321
6.0–6.5	$62.9^{+4.9}_{-4.7}$	$55.3^{+7.0}_{-6.5}$	$70.4^{+7.1}_{-6.7}$	155.2	0.310
6.5–7.0	$54.8^{+2.7}_{-2.6}$	$50.8^{+3.8}_{-3.7}$	$58.7^{+3.8}_{-3.7}$	134.3	0.289
7.0–7.5	$53.8^{+2.5}_{-2.4}$	$55.6^{+3.6}_{-3.5}$	$52.1^{+3.5}_{-3.3}$	117.1	0.271
7.5–8.0	$40.4^{+2.2}_{-2.1}$	$39.6^{+3.1}_{-3.0}$	$41.1^{+3.1}_{-2.9}$	101.2	0.257
8.0–8.5	$36.4^{+1.9}_{-1.8}$	$37.2^{+2.7}_{-2.6}$	$35.7^{+2.6}_{-2.5}$	85.8	0.240
8.5–9.0	$30.5^{+1.7}_{-1.6}$	$28.4^{+2.3}_{-2.2}$	$32.6^{+2.4}_{-2.2}$	71.7	0.223
9.0–9.5	$22.4^{+1.4}_{-1.3}$	$19.8^{+1.9}_{-1.8}$	$24.9^{+2.1}_{-1.9}$	58.5	0.205
9.5–10.0	$19.1^{+1.2}_{-1.2}$	$17.7^{+1.7}_{-1.6}$	$20.3^{+1.8}_{-1.7}$	47.1	0.186
10.0–10.5	$14.3^{+1.0}_{-1.0}$	$15.0^{+1.5}_{-1.4}$	$13.6^{+1.4}_{-1.3}$	37.0	0.169
10.5–11.0	$13.7^{+1.0}_{-0.9}$	$14.7^{+1.4}_{-1.3}$	$12.9^{+1.3}_{-1.2}$	28.5	0.151
11.0–11.5	$9.41^{+0.79}_{-0.73}$	$9.36^{+1.17}_{-1.03}$	$9.44^{+1.11}_{-0.98}$	21.45	0.134
11.5–12.0	$5.63^{+0.64}_{-0.57}$	$5.24^{+0.90}_{-0.76}$	$6.04^{+0.94}_{-0.81}$	15.76	0.118
12.0–12.5	$4.91^{+0.57}_{-0.50}$	$4.08^{+0.79}_{-0.66}$	$5.69^{+0.85}_{-0.73}$	11.21	0.102
12.5–13.0	$3.03^{+0.44}_{-0.38}$	$2.67^{+0.61}_{-0.49}$	$3.38^{+0.65}_{-0.53}$	7.79	0.088
13.0–13.5	$1.92^{+0.35}_{-0.29}$	$1.59^{+0.47}_{-0.35}$	$2.25^{+0.55}_{-0.43}$	5.22	0.074
13.5–14.0	$1.32^{+0.29}_{-0.23}$	$1.13^{+0.39}_{-0.27}$	$1.48^{+0.47}_{-0.35}$	3.39	0.062
14.0–15.0	$2.15^{+0.36}_{-0.30}$	$2.00^{+0.51}_{-0.40}$	$2.31^{+0.53}_{-0.42}$	3.49	0.092
15.0–16.0	$0.832^{+0.234}_{-0.175}$	$0.381^{+0.289}_{-0.158}$	$1.208^{+0.385}_{-0.275}$	1.227	0.059
16.0–20.0	$0.112^{+0.130}_{-0.064}$	$0.244^{+0.238}_{-0.117}$	$0.000^{+0.123}_{-0.401}$	0.513	0.068

APPENDIX B: PARAMETRIZED SURVIVAL PROBABILITY FIT

We fit the SK spectral data to the exponential, quadratic, and cubic survival probability in the same
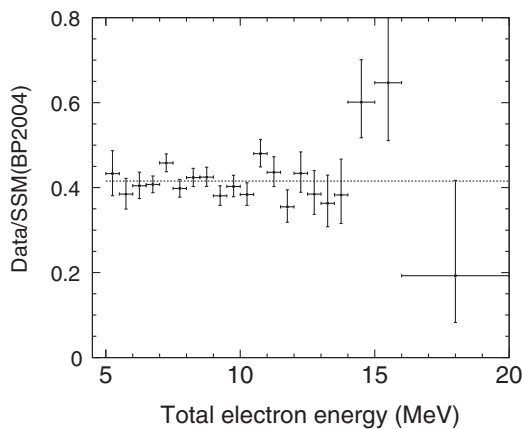

FIG. 38   Revised ratio of observed and expected energy spectra in SK-III. The dashed line represents the revised SK-III average. This is a revision of Fig. 27 in the previous paper [9].

manner as we fit them to the MSW prediction. Figure 39 shows the resulting allowed areas of the exponential coefficients e_1 and e_2. The "baseline" (average P_{ee}) e_0 is profiled; the e_0 constraint results from the comparison of the electron elastic scattering rate in SK and the SNO neutral-current interaction rate on deuterium. The contours deviate from a multivariate Gaussian. As there is no significant deviation from an undistorted spectrum, the data impose no constraint on e_2, the "steepness" of the exponential. Table XVII uses the best quadratic form approximation of the χ^2 of the fit as a function of the parameters to extract the values, uncertainties and correlations. Figure 40 shows the allowed shape parameters (c_1 and c_2) and the allowed slope (c_1) vs the baseline (c_0) of the quadratic fit. The SK-IV contours show some deviations from a multivariate Gaussian at 3σ, while the SK combined result is consistent with it. Overlaid in blue are the constraints from the SNO measurements. The corresponding coefficients of Table XVII differ slightly from those in [19] which fits both the survival probability to a quadratic function and the energy dependent day/night asymmetry to a linear function. Here, we
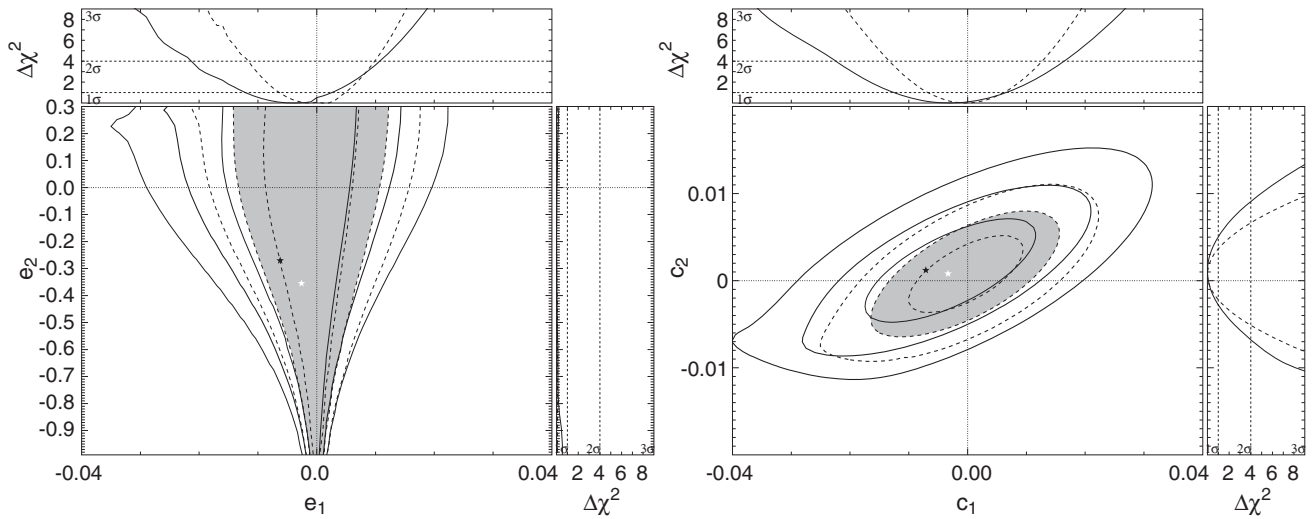
FIG. 39　Allowed areas of the shape parameters (e_1 and e_2 on left, c_1 and c_2 on the right) of an exponential (left) and quadratic (right) fit to the survival probability P_{ee} of SK-IV (solid lines) and all SK data (dashed lines) at the 1, 2 (filled region) and 3σ confidence levels. The oscillation parameter set corresponding to the SK (or all solar neutrino) data best-fit is indicated by the white star. The solar + KamLAND best-fit (black star) is also shown.

assume the energy dependence of the day/night effect calculated from standard earth matter effects. The resulting reduction in the degree of freedom leads to somewhat tighter constraints as well as a slight shift in the best fit value. The precision of the SK constraint is similar to that based on SNO data, and also statistically consistent.

Since SK's correlation between c_1 and c_2 is opposite to that of SNO's, a combined fit is rather powerful in constraining the shape. The $c_1 - c_2$ correlation is slightly smaller. The addition of SK data to SNO data not only significantly increases the precision of the c_0 determination, but the uncertainties on the shape are reduced.

TABLE XV　SK exponential and polynomial best-fit coefficients and their correlations. Also given are SNO's quadratic fit coefficients (slightly different than the published value since the day/night asymmetry is not fit) as well as SK and SNO combined measured quadratic fit coefficients and their respective correlations.

Data set	e_0	e_1	e_2	e_0-e_1 corr.			
SK-IV	0.326 ± 0.024	-0.0029 ± 0.0073	no constraint	$+0.202$			
SK	0.336 ± 0.023	-0.0014 ± 0.0051	no constraint	$+0.077$			

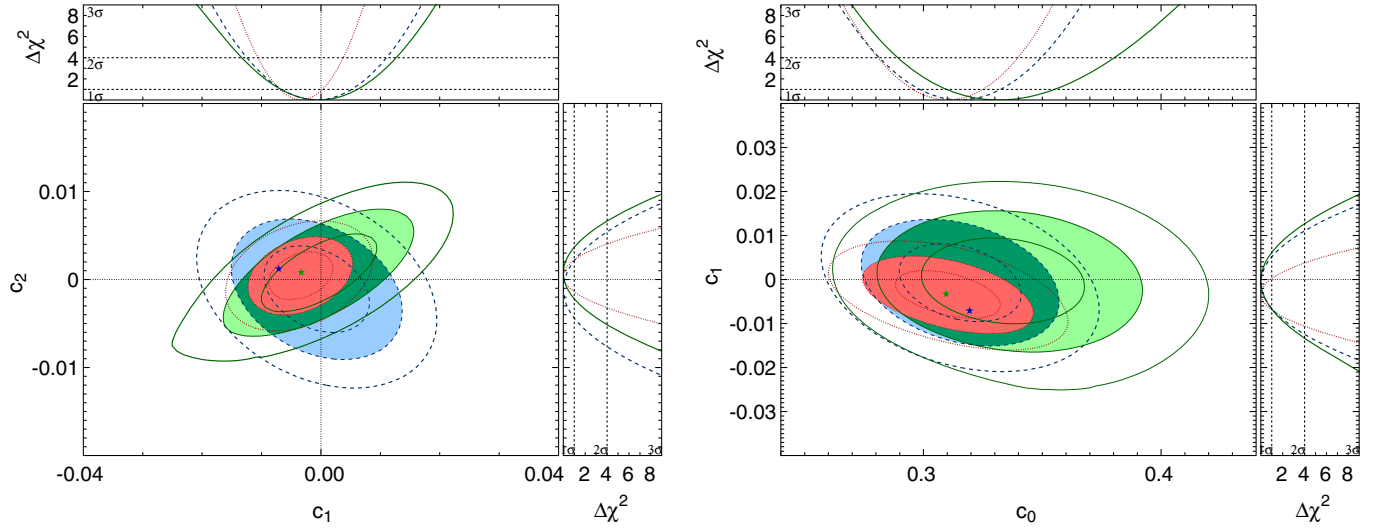|	quadratic function			cubic function			
	c_0	c_1	c_2	c_0	c_1	c_2	c_3
SK-IV	0.324 ± 0.025	-0.0030 ± 0.0097	0.0012 ± 0.0040	0.313 ± 0.028	-0.018 ± 0.021	0.0059 ± 0.0074	0.0021 ± 0.0028
c_0	1	-0.125	-0.412	1	$+0.388$	-0.602	-0.488
c_1	-0.125	1	$+0.6830$	$+0.388$	1	-0.580	-0.892
c_2	-0.412	$+0.683$	1	-0.602	-0.580	1	$+0.839$
c_3				-0.488	-0.892	$+0.839$	1
SK	0.334 ± 0.023	-0.0003 ± 0.0065	0.0008 ± 0.0029	0.313 ± 0.024	-0.031 ± 0.016	0.0097 ± 0.0051	0.0044 ± 0.0020
c_0	1	-0.131	-0.345	1	$+0.258$	-0.449	-0.327
c_1	-0.131	1	$+0.649$	$+0.258$	1	-0.599	-0.916
c_2	-0.345	$+0.649$	1	-0.449	-0.599	1	$+0.814$
c_3				-0.327	-0.916	$+0.814$	1
				c_0-c_1 corr.	c_0-c_2 corr.	c_1-c_2 corr.	
SNO	0.315 ± 0.017	-0.0007 ± 0.0059	-0.0011 ± 0.0033	-0.301	-0.391	-0.312	
SK + SNO	0.311 ± 0.015	-0.0034 ± 0.0036	$+0.0004 \pm 0.0018$	-0.453	-0.407	$+0.301$	

FIG. 40.   Left: Allowed areas of the shape parameters (c_1 and c_2) of a quadratic fit to the survival probability P_{ee} of SK (solid green) and SNO (dashed blue) data at the 1, 2 (filled region) and 3σ confidence levels. Right: Allowed areas of the slope (c_1) and baseline (c_0) of a quadratic fit to the survival probability P_{ee} of SK (solid green) and SNO (dashed blue) data at the 1, 2 (filled region) and 3σ confidence levels. Also shown is a combined fit (dotted red). The oscillation parameter set corresponding to the SK (all solar neutrino) data best-fit is indicated by the dark green (light blue) star. The solar + KamLAND best-fit (dark blue) is also shown.

APPENDIX C: TABLES

TABLE XVI   The observed event rates in each energy bin (events/year/kton), at 1 AU. The errors are statistical errors only. The reduction efficiencies are corrected and the expected event rates are for a flux of $5.25 \times 10^6/(\text{cm}^2 \text{ sec})$.

Energy (MeV)	ALL $-1 \leq \cos\theta_z \leq 1$	Observed rate DAY $-1 \leq \cos\theta_z \leq 0$	NIGHT $0 < \cos\theta_z \leq 1$	Expected rate ^{8}B	*hep*
3.49–3.99	$92.2^{+10.8}_{-10.6}$	$96.0^{+16.8}_{-16.3}$	$81.5^{+14.0}_{-13.6}$	196.8	0.346
3.99–4.49	$76.7^{+5.2}_{-5.1}$	$64.6^{+7.9}_{-7.6}$	$85.2^{+6.9}_{-6.7}$	182.8	0.335
4.49–4.99	$82.1^{+3.4}_{-3.3}$	$79.4^{+5.1}_{-5.0}$	$84.6^{+4.6}_{-4.5}$	167.8	0.323
4.99–5.49	$69.3^{+2.1}_{-2.1}$	$65.9^{+3.1}_{-3.0}$	$72.5^{+3.0}_{-2.9}$	153.3	0.312
5.49–5.99	$59.6^{+1.6}_{-1.6}$	$58.3^{+2.3}_{-2.2}$	$60.5^{+2.2}_{-2.2}$	137.8	0.298
5.99–6.49	$54.2^{+1.4}_{-1.4}$	$51.0^{+2.1}_{-2.0}$	$56.9^{+2.0}_{-2.0}$	121.9	0.282
6.49–6.99	$47.8^{+1.3}_{-1.3}$	$45.7^{+1.9}_{-1.8}$	$49.9^{+1.9}_{-1.8}$	106.8	0.266
6.99–7.49	$40.6^{+1.2}_{-1.1}$	$41.8^{+1.7}_{-1.7}$	$39.5^{+1.6}_{-1.6}$	92.1	0.250
7.49–7.99	$35.7^{+1.0}_{-1.0}$	$35.0^{+1.5}_{-1.5}$	$36.1^{+1.5}_{-1.4}$	78.0	0.232
7.99–8.49	$29.1^{+0.9}_{-0.9}$	$28.6^{+1.3}_{-1.3}$	$28.9^{+1.3}_{-1.2}$	65.2	0.214
8.49–8.99	$24.0^{+0.8}_{-0.8}$	$24.1^{+1.2}_{-1.1}$	$23.7^{+1.1}_{-1.1}$	53.4	0.197
8.99–9.49	$18.5^{+0.7}_{-0.7}$	$17.9^{+1.0}_{-0.9}$	$19.2^{+1.0}_{-0.9}$	42.9	0.179
9.49–9.99	$14.5^{+0.6}_{-0.6}$	$14.5^{+0.9}_{-0.8}$	$14.4^{+0.8}_{-0.8}$	33.8	0.162
9.99–10.5	$10.7^{+0.5}_{-0.5}$	$10.2^{+0.7}_{-0.7}$	$11.1^{+0.7}_{-0.7}$	26.0	0.144
10.5–11.0	$8.43^{+0.43}_{-0.41}$	$7.73^{+0.61}_{-0.56}$	$9.23^{+0.64}_{-0.60}$	19.55	0.128
11.0–11.5	$6.60^{+0.37}_{-0.35}$	$6.60^{+0.54}_{-0.49}$	$6.72^{+0.53}_{-0.49}$	14.34	0.112
11.5–12.0	$4.40^{+0.30}_{-0.28}$	$3.83^{+0.41}_{-0.37}$	$4.89^{+0.44}_{-0.40}$	10.24	0.097
12.0–12.5	$3.04^{+0.25}_{-0.23}$	$3.04^{+0.35}_{-0.31}$	$3.06^{+0.36}_{-0.32}$	7.10	0.083
12.5–13.0	$2.14^{+0.20}_{-0.18}$	$2.41^{+0.31}_{-0.27}$	$1.93^{+0.29}_{-0.25}$	4.80	0.070
13.0–13.5	$1.47^{+0.17}_{-0.15}$	$1.48^{+0.25}_{-0.21}$	$1.47^{+0.25}_{-0.21}$	3.11	0.059
13.5–14.5	$1.59^{+0.17}_{-0.15}$	$1.54^{+0.25}_{-0.21}$	$1.63^{+0.25}_{-0.22}$	3.18	0.088
14.5–15.5	$0.469^{+0.102}_{-0.082}$	$0.486^{+0.151}_{-0.112}$	$0.493^{+0.161}_{-0.121}$	1.117	0.056
15.5–19.5	$0.186^{+0.072}_{-0.051}$	$0.150^{+0.108}_{-0.065}$	$0.203^{+0.113}_{-0.071}$	0.464	0.064

TABLE XVII Elastic scattering rate ratios and energy-uncorrelated uncertainties (statistical plus systematic) for each SK phase.

Energy (MeV)	SK-I	SK-II	SK-III	SK-IV
3.49–3.99	–	–	–	$0.468^{+0.060}_{-0.059}$
3.99–4.49	–	–	$0.448^{+0.100}_{-0.096}$	0.419 ± 0.030
4.49–4.99	$0.453^{+0.043}_{-0.042}$	–	$0.472^{+0.058}_{-0.056}$	0.488 ± 0.023
4.99–5.49	$0.430^{+0.023}_{-0.022}$	–	$0.420^{+0.039}_{-0.037}$	0.451 ± 0.014
5.49–5.99	0.449 ± 0.018	–	$0.457^{+0.035}_{-0.034}$	0.432 ± 0.012
5.99–6.49	0.444 ± 0.015	–	$0.433^{+0.023}_{-0.022}$	0.444 ± 0.015
6.49–6.99	$0.461^{+0.016}_{-0.015}$	$0.439^{+0.050}_{-0.048}$	$0.504^{+0.025}_{-0.024}$	0.447 ± 0.015
6.99–7.49	0.476 ± 0.016	$0.448^{+0.043}_{-0.041}$	$0.424^{+0.024}_{-0.023}$	0.440 ± 0.015
7.49–7.99	$0.457^{+0.017}_{-0.016}$	$0.461^{+0.037}_{-0.036}$	$0.467^{+0.024}_{-0.023}$	0.455 ± 0.014
7.99–8.49	$0.431^{+0.017}_{-0.016}$	$0.473^{+0.036}_{-0.035}$	$0.469^{+0.026}_{-0.025}$	$0.439^{+0.015}_{-0.014}$
8.49–8.99	$0.454^{+0.018}_{-0.017}$	$0.463^{+0.036}_{-0.034}$	$0.420^{+0.026}_{-0.025}$	$0.445^{+0.016}_{-0.015}$
8.99–9.49	0.464 ± 0.019	$0.499^{+0.038}_{-0.037}$	$0.444^{+0.029}_{-0.027}$	0.430 ± 0.016
9.49–9.99	$0.456^{+0.021}_{-0.020}$	$0.474^{+0.038}_{-0.036}$	$0.423^{+0.031}_{-0.029}$	$0.426^{+0.018}_{-0.017}$
9.99–10.5	0.409 ± 0.021	$0.481^{+0.041}_{-0.039}$	$0.529^{+0.037}_{-0.035}$	$0.408^{+0.019}_{-0.018}$
10.5–11.0	$0.472^{+0.025}_{-0.024}$	$0.452^{+0.043}_{-0.040}$	$0.481^{+0.041}_{-0.037}$	$0.432^{+0.023}_{-0.021}$
11.0–11.5	$0.439^{+0.028}_{-0.026}$	$0.469^{+0.046}_{-0.043}$	$0.391^{+0.044}_{-0.040}$	$0.461^{+0.026}_{-0.025}$
11.5–12.0	$0.460^{+0.033}_{-0.031}$	$0.482^{+0.052}_{-0.048}$	$0.479^{+0.055}_{-0.049}$	$0.423^{+0.029}_{-0.027}$
12.0–12.5	$0.465^{+0.039}_{-0.036}$	$0.419^{+0.054}_{-0.049}$	$0.425^{+0.061}_{-0.053}$	$0.425^{+0.035}_{-0.032}$
12.5–13.0	$0.461^{+0.048}_{-0.043}$	$0.462^{+0.063}_{-0.057}$	$0.400^{+0.073}_{-0.061}$	$0.445^{+0.043}_{-0.039}$
13.0–13.5	$0.582^{+0.064}_{-0.057}$	$0.444^{+0.070}_{-0.062}$	$0.422^{+0.093}_{-0.074}$	$0.465^{+0.055}_{-0.049}$
13.5–14.5	$0.475^{+0.059}_{-0.052}$	$0.430^{+0.066}_{-0.059}$	$0.663^{+0.110}_{-0.093}$	$0.485^{+0.054}_{-0.048}$
14.5–15.5	$0.724^{+0.120}_{-0.102}$	$0.563^{+0.100}_{-0.087}$	$0.713^{+0.201}_{-0.150}$	$0.418^{+0.090}_{-0.074}$
15.5–19.5	$0.575^{+0.173}_{-0.130}$	$0.648^{+0.123}_{-0.103}$	$0.212^{+0.248}_{-0.122}$	$0.338^{+0.140}_{-0.099}$

[1] J. Hosaka *et al.*, Phys. Rev. D **73**, 112001 (2006).
[2] Q. R. Ahmad *et al.* (The SNO Collaboration), Phys. Rev. Lett. **87**, 071301 (2001).
[3] S. Abe *et al.*, Phys. Rev. Lett. **100**, 221803 (2008); A. Gando *et al.* (The KamLAND Collaboration), Phys. Rev. D **88**, 033001 (2013).
[4] S. P. Mikheyev and A. Y. Smirnov, Sov. J. Nucl. Phys. **42**, 913 (1985); L. Wolfenstein, Phys. Rev. D **17**, 2369 (1978).
[5] A. Friedland, C. Lunardini, and C. Peña-Garay, Phys. Lett. B **594**, 347 (2004).
[6] R. Fardon, A. E. Nelson, and N. Weiner, J. Cosmol. Astropart. Phys. 10 (2004) 005; M. Cirelli, M. C. Gonzalez-Garcia, and C. Peña-Garay, Nucl. Phys. **B719**, 219 (2005).
[7] Y. Fukuda *et al.*, Nucl. Instrum. Methods Phys. Res., Sect. A **501**, 418 (2003).
[8] J. P. Cravens *et al.*, Phys. Rev. D **78**, 032002 (2008).
[9] K. Abe *et al.*, Phys. Rev. D **83**, 052010 (2011).
[10] H. Nishino *et al.*, Null. Instrum. Methods Pays. Res. Sect. A **610**, 710 (2010); S. Yamada *et al.* IEEE Trans. Nucl. Sci. 57, **428** (2010).
[11] K. Abe *et al.*, Nucl. Instrum. Methods Phys. Res., Sect. A **737** 253 (2014).
[12] M. Nakahata *et al.*, Nucl. Instrum. Methods Phys. Res., Sect. A **421**, 113 (1999).
[13] E. Blaufuss *et al.*, Nucl. Instrum. Methods Phys. Res., Sect. A **458**, 638 (2001).
[14] Y. Nakano, Ph.D. thesis, University of Tokyo, 2016; http://www-sk.icrr.u-tokyo.ac.jp/sk/publications/index-e.html.
[15] S. W. Li and J. F. Beacom, Phys. Rev. C **89**, 045801 (2014), Phys. Rev. D **91**, 105005 (2015).
[16] Y. Zhang *et al.*, Phys. Rev. D **93**, 012004 (2016).
[17] W. T. Winter, S. J. Freedman, K. E. Rehm, and J. P. Schiffer, Phys. Rev. C **73**, 025503 (2006).
[18] J. N. Bahcall, M. Kamionkowski, and A. Sirlin, Phys. Rev. D **51**, 6146 (1995).

[19] B. Aharmin *et al.*, Phys. Rev. C **88**, 025501 (2013).

[20] B. Aharmim *et al.*, Astrophys. J. **653**, 1545 (2006).

[21] J. N. Bahcall, A. M. Serenelli, and S. Basu, Astrophys. J. Suppl. Ser. **165**, 400 (2006).

[22] R. Davis, Jr., D. S. Harmer, and K. C. Hoffman (Homestake Experiment), Phys. Rev. Lett. **20**, 1205 (1968); J. N. Abdurashitov *et al.* (SAGE collaboration), Phys. Rev. C **80**, 015807 (2009); M. Altmann *et al.* (GALLEX Collaboration), Phys. Lett. B **616**, 174 (2005); G. Bellini *et al.* (Borexino Collaboration), Phys. Rev. Lett. **107**, 141302 (2011).

[23] Bellini *et al.* Phys. Rev. D **82**, 033006 (2010); Phys. Rev. Lett. **108**, 051302 (2012).

[24] M. B. Smy *et al.*, Phys. Rev. D **69**, 011104(R) (2004).

[25] F. P. An *et al.* (Daya Bay Collaboration), Chin. Phys. C **37**, 011001 (2013); J. K. Ahn *et al.*, Phys. Rev. Lett. **108**, 191802 (2012); Y. Abe *et al.*, Phys. Rev. D **86**, 052008 (2012).

[26] A. M. Dziewonski and D. L. Anderson, Phys. Earth Planet. Inter. **25**, 297 (1981).

[27] J. J. Durek and G. Ekstrom, Bull. Seismol. Soc. Am. **86**, 144 (1996).

[28] A. Renshaw *et al.*, Phys. Rev. Lett. **112**, 091805 (2014).

[29] G. Bellini *et al.*, Phys. Lett. B **707**, 22 (2012).